



Supplementary Information for

Seasonally-resolved stratigraphy at Jwalapuram, India shows regional surface warming after the Toba volcanic super-eruption

Gopesh Jha^{1,2,3*}, Mafalda Costa^{2,4}, Anna Tsoupra², Cristina Barrocas Dias^{2,4,5}, Ola Kwiecien⁶, Jack Longman⁶, Sebastian F. M. Breitenbach⁶, Peter Ditchfield⁷, Deepak Kumar Jha⁸, Rachel Rudd⁸, Devara Anilkumar⁹, Roshan Paladugu¹⁰, Sindu Shree¹¹, Hema Achyuthan¹², Rachna Raj¹³, K. Krishnan^{9*}, Nicole Boivin^{1,14,15*}, Patrick Roberts^{1,8*}, Michael Petraglia^{15,16,17*}

Corresponding author(s): Gopesh Jha, K. Krishnan, Nicole Boivin, Patrick Roberts, Michael Petraglia.

Email: gjha@gea.mpg.de

This PDF file includes:

Supplementary text
Figures S1 to S33
Tables S1 to S4

Other supplementary materials for this manuscript include the following:

Datasets S1 – Geochemical dataset

Supplementary Information Text

1. Stratigraphic observations

The current work focuses on unit C: the tephra (YTT) deposit of the Jwalapuram site (fig. S1), specifically at two localities (JWP3 and JWP2020) that exhibit a similar stratigraphic sequence (see figs. 2, S2, and S3; table S1). The stratigraphic sequence at JWP3 and JWP2020 consists of four layers — layer A to layer D. Table S1 summarizes the YTT-bearing sequence (figs. S2

and S3 and table S1). Here, we present a detailed stratigraphic description of layer C (YTT), discussing its three main components: (1) Primary YTT, (2) redeposited YTT, and (3) hardpan. For more information on the lithological descriptions, refer to Petraglia et al.(1, 2), Jones et al. (3), and Haslam et al.(4, 5).

1a. Primary ashfall

A distinct ~5 cm layer of volcanic ash (base of unit C1) is evident in the basal levels of layer C at several localities near JWP3 and JWP2020 (figs. S2, S3, and S5), differing slightly from the overlying tephra deposits(1–4). This compact, slightly darker layer contrasts with the overlying tephra and is separated by a thin, discontinuous band of reddish-brown sediment (fig. S4)(3). The interface between the primary YTT and the underlying reddish-brown paludal clay horizon contains soft-sediment deformation and pellet-like structures (fig. S4)(3, 4). "Veins" of reddish-brown sediment within this YTT layer and the overlying bands and specks suggest sediment "bleeding" over the primary ash layer after settling, and displacement of loose sediment into the aquatic setting (fig. S4)(3, 4). The "swirls" and rippling features at the top of the primary ash indicate localized gentle currents deforming the ash surface or disturbance from the influx of overlying reworked ash into the water (fig. S6) (3, 4). The "pellets" may result from ash particle aggregation during water deposition or from diagenetic or biogenic processes, possibly from microbial activity or as faecal pellets or casts of burrowing organisms (3, 4). Granulometric data shows that the basal YTT layer possesses a higher proportion of finer grains compared to the overlying tephra layers (fig. S18)(3). These stratigraphic observations suggest that the initial YTT deposition occurred in an aqueous environment(3, 4, 6). Previous studies indicate that the volcanic ash layer at the base of unit C1 likely represents primary air-fall ash, with its thickness matching primary ash layers preserved in Indian Ocean marine cores (1–4, 7).

1b. YTT redeposition

The litho-stratigraphic sequence at JWP3, JWP23, and JWP2020 reveals six distinct units (C1–C6) of tephra, representing six separate tephra deposition events in the Jurreru basin (figs. 2 and S2). Each unit is characterized by relatively pure tephra deposits, lacking coarse autochthonous terrigenous material (figs. 4 and S6)(3, 4). Common sedimentological features across all tephra units include a distinct type of rippling structure, suggesting ash redeposition in water and preservation in low-energy conditions (figs. S4 and S6) (3, 4). The tephra units consistently exhibit upward-fining sediments, topped by a continuous hardpan with mud cracks and fossil plant remains (figs. S7 – S15) (3, 4). The YTT layers (unit C) shows signs of insect burrows, root casts, and other biogenic structures, with rhizoliths extending vertically through the tephra (figs. S10 S13, and S14) (3, 4). These root casts vary in morphology and preservation, with some lithified by silica and carbonate, appearing pale grey to pale brownish-grey (figs. S10, S13, and S14) (3, 4).

Beyond root fossils, abundant evidence of in-situ plant/tree fossils were observed in the area, stratigraphically associated with the YTT horizon (figs. S7, S8, and S9) (3, 4, 8). Several in-situ fossilized tree trunks have been identified at sites JV7, JV32, and JV21 (figs. 7 and 8)(8). The exceptional preservation of these tree fossils is likely related to their rapid burial by massive quantities of YTT ash. While the branching structures of these tree fossils are visible in stratum C (fig. S8), no fossils are preserved in the sediments above the tephra layer (i.e., layer A and B)(8). Many of these fossils are rooted in the sediments below the YTT horizon, suggesting that they reflect organisms that were alive at the time of the primary Toba ash fall in the Jurreru Valley(6, 8).

Additionally, excavations at JV7 revealed numerous fossil leaf casts at the interface between the primary ash fall layer and the overlying reworked tephra deposits (fig. S9). The presence

of leaf fall on top of the primary ash layer has been linked to a possible defoliation event caused by the toxic effects of the ashfall on the trees(6, 8). The morphology of these samples indicates the presence of both palmate and pinnate species (6, 8). Another significant feature in all tephra units is the presence of mud cracks (fig. S15), resulting from the rapid drying of tephra, leading to the development of cracks and the transportation of finer clayey material(3, 4).

1c. Hardpan

Five brownish-grey hardpans, ranging in thickness from approximately 5 to 20 mm, are preserved within the tephra unit (layer C) at JWP2020 and JWP3 (fig. S11)(3, 4). These hardpans are mostly horizontal, although some undulation of the surfaces is apparent (fig. S12)(3, 4). They are continuous in the topographically low-lying sections where the YTT deposit is thickest (3, 4). However, in areas with thinner YTT deposits, such as near the dam and hill slopes, these hardpans are less distinct, discontinuous, or often missing(3, 4). The upper surface of the hardpan exhibits a mosaic of ichnofossils, including large roots and burrows (figs. S12 and S13)(3, 4). The hardpans also contain horizontal and vertical mud cracks, primarily formed due to the desiccation of the topmost tephra surface, a common feature observed during the rapid drying of lake or swamp surfaces(9, 10). Many of these root cast traces are surrounded by black Fe-Mn stains (fig. S12), indicating former microbial activity on the hardpan surfaces(3, 7). Additionally, several horizontal rhizoliths and sub-rounded termitaria were observed on the surfaces of the hardpans (figs. S12, S13, and S16).

2. Chronology

Our work builds upon the earlier evidence outlined in Petraglia et al.(1), Jones et al.(3), and Haslam et al.(4), based on micro-stratigraphic observations and sedimentological analyses of YTT deposits at Jwalapuram. It was previously argued that the six units of Toba ash were deposited over six monsoon seasons (annual cycles), where each couplet of tephra (wet) and

hardpan (dry) represents a single monsoonal cycle (fig. 7 and S2)(1, 3, 4). Stratigraphic observations such as ripple and swirling marks, upward fining, and laminations—suggested that all tephra units were deposited in a wet environment, likely by sheet wash and colluvial processes such as slumping (figs. S4 and S6). Other features such as mud cracks, burrowing, hardpan (dolocrete) formation, and the development of microbial mats—indicate desiccation and increasing warmth after each wet period (figs. S6, S12, and S15). These stratigraphic observations highlight oscillating wet-dry conditions, likely related to monsoonal cyclicity(1, 3, 4).

Key features, such as the in-situ burial of tree trunks, leaf imprints, and a higher density of detrital matter, indicate an exceptional preservation environment facilitated by the rapid mobilization and burial of local vegetation (figs. S1, S7, S8, and S9)(3, 7, 8). Strongly correlated granulometric (PDA) data, magnetic susceptibility, carbonate content (%), and total organic matter (TOM %) present similar inferences about the temporality of the YTT deposit at Jwalapuram (fig. S18)(3). For instance, each tephra deposition episode is marked by a relative increase in TOM and a decrease in carbonate concentration, which is inversely reflected in the hardpan layers, again demonstrating an oscillating wet-dry pattern (fig. S18).

The current geochemical dataset contributes to, and strengthens, this argument. Our multi-proxy dataset highlights no major change in the geochemical composition of the Toba tephra, suggesting that all units of tephra are relatively pure and show no signs of mixing with autochthonous terrigenous material (fig. 4 and S24). Similar observations were made based on PDA data, highlighting the exceptional purity of Toba ash in Jwalapuram, likely due to rapid mobilization and deposition(3). We compare distribution patterns among our palaeopedological and palaeoenvironmental proxies and modern seasonal (temperature and rainfall) records.

We suggest that the sinusoidal pattern observed in palaeoprecipitation (Rb/Sr and ΔMAP) and stable isotope proxies (i.e., $\delta^{13}\text{C}_{\text{PC}}$, $\delta^{18}\text{O}_{\text{PC}}$, and $\delta^{13}\text{C}_{\text{SOM}}$) highlights climate seasonality, represented by minima and maxima of climatic factors such as precipitation and temperature (fig. S17)(11). For example, relatively higher Rb/Sr values in the tephra units and lower values in the hardpan also point towards seasonal oscillation in precipitation(12, 13). Similarly, the increasing concentration of evaporites (i.e. dolomite) in the hardpan and the comparatively lower concentration in the tephra units indicate fluctuations in evaporative conditions, likely related to seasonal temperature changes(10, 14, 15). Thus, the evidence strongly supports that the six sub-units of Toba tephra at Jwalapuram represent six annual monsoonal cycles, likely representing six years following the YTT event(1, 3, 4, 6). However, it is important to acknowledge that these assertions cannot be backed by absolute chronometric ages due to the inability of current chronometric methods to provide ages of such fine resolution. Nonetheless, there are numerous examples of historical volcanic eruptions that have shown similar depositional phenomena.

Freshly deposited unconsolidated primary air-fall volcanic tephra is prone to erosion due to factors such as landscape gradient, climatic conditions, and vegetation(16–19). Several case studies from different volcanic landscapes across the globe have shown that subsequent rainfall seasons after primary ashfall lead to rapid mobilization of tephra, primarily due to sheet wash, rill erosion, and simultaneous aeolian activity, resulting in the slumping of tephra into topographic low-lying regions like lakes, ponds, and valleys(20–30). Recurrent mobilization of tephra in subsequent rainy seasons (following annual cycles) leads to the formation of multiple laminated reworked tephra layers resting on the primary tephra deposit(21, 28, 31).

One key example of seasonal/annual reworking of Toba tephra was observed at the YTT site of Kampung Luat 3 in the Lenggong Valley, Malaysia(31). Gatti et al.(31) argued, based on stratigraphic, sedimentological, and geochemical data, that the two layers of relatively pure

Toba tephra represent two rainy seasons, demarcated by two hardpan layers which are markers of the dry season (fig. 7). Beyond the case of Toba, this phenomenon of annual or seasonal reworking of tephra is commonly observed in different terrestrial records in volcanic landscapes across the globe.

The following are examples:

- **Parícutin eruption, Mexico (1943-1952)** - Bolos et al.(22) showed multiple episodes of tephra remobilization due to seasonal fluvial activity (slope wash) and lahar, resulting in multi-annual deposits of interbedded primary and secondary tephra in low-lying regions.
- **Mt. Helens eruption, USA (1980)** - Three years of intense tephra mobilization and reworking were observed after the eruption, leading to the deposition of annually deposited tephra layers in surrounding lakes(30).
- **Hekla eruption, Iceland (1947)** - Seasonal ablation of freshly deposited tephra on glacial surfaces was observed, particularly during summer seasons, which led to the seasonal/annual slumping of tephra into local lakes lasting for several years(28).
- **Dawson tephra, Yukon, Canada (25.3 ka)** - Recurrent transportation of tephra from hillslopes to riparian areas during subsequent spring seasons after the primary ashfall. Annual reworking of tephra deposits on glacial surfaces during spring resulted in multiple upward-fining tephra-rich frozen sediment beds spanning several years(32).
- **Campanian Ignimbrite (CI) deposit, Lago Grande di Monticchio, Italy (39.3 ka)** - The 100 kyr lacustrine deposit of Lake Monticchio contains 340 distal tephra layers, representing 26 volcanic events. Seven CI tephra layers present an interesting story of environmental impact. Wutke et al. demonstrated annual reworking of tephra, lasting for eight years after primary deposition(25, 33, 34).

The aforementioned examples demonstrate that seasonal or annual reworking and redeposition of tephra in terrestrial settings occurs frequently. Thus, our study supports earlier arguments suggesting that the Toba tephra deposit at Jwalapuram represents six annual cycles (i.e., six years) after the primary YTT deposition, providing a rare temporal snapshot immediately after the largest volcanic eruption of the Quaternary (~74 ka YTT event).

3. Chemical weathering proxies

Primary rock-forming elements are often called "major elements", such as Ca, Fe, K, Mg, Na, Al, Si, Mn, P, and Ti(35). Among these, Ca, Mg, Na, and K are considered base elements susceptible to weathering(12, 36). A remarkable degree of mobility is noticed among base elements due to increasing chemical weathering(36, 37). On the contrary, other significant elements like Al, Si, Fe, Mn, and Ti are considered to be fairly immobile and resistant to chemical alteration(36, 37). These alterations cause variation in mobility and immobility patterns, reflected in the enrichment and depletion of elemental concentrations(37). Elemental ratios of mobile and immobile elements are widely used to explain paedogenic processes (tables S2 and S3), such as hydrolysis, leaching, acidification, and salinization(37). Most of these processes are climate sensitive and explain the nature of post-depositional alteration of silicate minerals(36, 38–41).

Apart from major element ratios, different chemical weathering and alteration indices are used to understand the intensity of weathering and the role of climatic factors (i.e. precipitation and temperature) in paedogenic processes(36, 38, 42–45). Different weathering indices focus on the mobility of various major and minor elements and how other compounds or mineralogical groups undergo chemical transformations due to their mobility(36, 37). Due to harsh weathering, silicate minerals (tephra in this study) disintegrate, and silica is partially leached, resulting in the deposition of residual and new sesquioxides(12, 46, 47). These relative

variations of various elements can be used to understand the intensity of chemical weathering/alteration and act as critical palaeoenvironmental proxies(37, 38, 40, 41). The current study uses chemical index of alteration (CIA), chemical index of weathering (CIW), plagioclase index of alteration (PIA), and feldspar dissolution (f_{diss}), mainly focusing on weathering of silicate minerals in YTT(36, 37, 42, 48). Deng et al. suggest CIA and f_{diss} are strongly correlated to temperature, explaining the climatic context behind the mobility of base cations and feldspar hydrolysis (39–41, 49, 50). Table S2 and S3 explains the basic principle, formula, and application of major elemental ratios and weathering indices.

4. Palaeoclimate Proxy Justification

We employed a constellation of geochemical proxies to explore the paleoclimatic context of chemical weathering of tephra-derived silicate minerals and the formation of secondary minerals in order to understand palaeoenvironmental changes immediately following the ~74 ka YTT eruption at Jwalapuram.

4.1 Chemical weathering of tephra:

Chemical weathering of tephra involves the alteration of volcanic glass and primary minerals through interactions with water and atmospheric as well as pedogenic gases(16, 27, 28, 30, 53, 54, 58–61). This process is driven by the thermodynamic instability of tephra components in surface conditions, leading to dissolution and the subsequent formation of secondary minerals(12, 53, 54, 62, 63). Freshly deposited air-fall tephra is susceptible to rapid physical and chemical transformation which is significantly influenced by environmental factors, particularly precipitation and temperature(23, 27, 28). Studies in volcanic regions like Iceland have shown that fresh tephra undergoes rapid weathering during the rainy season, characterized by the dissolution of primary minerals and the formation of secondary minerals such as clays, carbonates, and oxides(28, 47, 60, 63).

This chemical weathering is accompanied by physical processes such as vegetation growth and other biogenic processes, which contribute to the mechanical breakdown of tephra particles(23, 47, 60). The rate and extent of weathering are influenced by factors such as tephra composition, particle size, climate, and water chemistry(27, 53). In basaltic and rhyolitic tephra, for example, the breakdown of silicate minerals releases cations like Ca, Mg, and Fe, which can form clay minerals and oxides(12, 59, 63). The presence of organic acids from vegetation can accelerate this process(23). Hydrolysis plays a key role, with water molecules breaking chemical bonds in minerals, while oxidation contributes to the formation of iron oxides, and leaching leads to the formation of secondary carbonate minerals.

Several studies have demonstrated that tephra and its mineral components can undergo dissolution immediately after deposition, likely due to exposure to water(16, 22, 28, 30, 54, 58, 60, 64). A field study of freshly deposited tephra from the 1980 Mt. Helens eruption showed rapid chemical weathering of tephra, leading to the loss of base elements and the formation of secondary minerals on the upper tephra surface(30, 54). These processes of tephra dissolution and precipitation of secondary minerals occurred annually. Similar instances of rapid chemical weathering of tephra were observed in Moanatuatua bog, New Zealand, where hyper-leaching of Ca, Mg, and P from tephra-derived minerals like biotite and apatite was noticed(65). Furthermore, hydrolysis and leaching experiments of andesitic tephra (similar to YTT) from the 2005 Talang eruption (Indonesia) showed rapid (within two months) loss of base cations due to feldspar dissolution(12). These experiments also showed the leaching of phosphorus and sulfur, demonstrating that cyclical wetting could lead to the dissolution of silicate minerals and warming could mobilize and precipitate leached elements (Ca, Mg, P, S) to form secondary minerals(12). An illustrative example of Ca and Mg leaching from tephra can be observed in volcanic regions like the Pacific Northwest of the United States, where Mount St. Helens erupted in 1980(30, 54). The eruption deposited a significant layer of tephra over the

surrounding landscape. In this region, the seasonal rainfall patterns, characterized by wet winters and dry summers, play a crucial role in the leaching process. During the wet winter months, increased rainfall leads to higher water percolation rates through the tephra layer, facilitating the leaching of Ca and Mg from the tephra into the soil profile (30, 54).

Our current research focuses on the concentration of mobile elements such as CaO, MgO, P₂O₅, S, and Sr that leached during hydrolysis of original glass and mineral components (primarily feldspar and biotite) in the YTT. An increase in the concentration of these elements could suggest increasing intensity of chemical weathering with significant palaeoclimatic implications (53). Furthermore, we compare the mobility of these elements against immobile elements like Al₂O₃ and TiO₂, which are relatively resilient to chemical alteration. Ratios like $\Sigma_{\text{Bases}}/\text{Al}_2\text{O}_3$ and $\Sigma_{\text{Bases}}/\text{TiO}_2$ provide insights into the intensity of hydrolysis and leaching of tephra-derived silicate minerals. Additionally, we calculated multiple indices such as the chemical index of alteration (CIA), chemical index of weathering (CIW), and plagioclase index of alteration (PIA) to understand the loss of base elements and dissolution intensity of siliciclastic minerals like feldspar.

4.2 Palaeoprecipitation proxies

Rb/Sr Ratio: The Rb/Sr ratio in tephra is a valuable proxy for reconstructing palaeoprecipitation patterns due to the distinct geochemical behaviour of rubidium (Rb) and strontium (Sr) during weathering processes (13, 53). Rb is typically less mobile due to its resilience to chemical leaching, whereas Sr is more easily leached under wetter conditions. When tephra weathers, it releases Sr along with other elements into the soil solution. This Sr can be transported by water, particularly during the rainy season, leading to its mobility in the soil profile. In semi-arid and arid environments, where calcrete (dolocrete in this case) crusts commonly form, the evaporation of soil moisture can lead to the precipitation of carbonates incorporating leached

Sr due to ion exchange and substitution processes (12, 53, 66). The high temperatures and arid conditions favour the concentration of dissolved ions, including Sr, which can then precipitate as part of the calcrete matrix (12, 53, 66). The incorporation of Sr into calcrete is facilitated by its chemical similarity to calcium (Ca), allowing Sr to substitute for Ca in carbonate minerals (12, 53). At Jwalapuram, lower Rb/Sr values indicate drying and strong evaporative conditions, while higher values correspond to relatively wetter environments (66).

4.3 Palaeotemperature and palaeoevaporation proxies

Dolomite precipitation is sensitive to temperature, with rising temperatures generally favouring its formation (67). Arvidson and Mackenzie (68) found that dolomite precipitation varies in composition within a temperature range of 25 to 200°C. The pH of the precipitating medium, controlled by carbonate ion concentration, is a crucial factor affecting dolomite precipitation (15, 69). Evapotranspiration plays a significant role in concentrating ions in soil solutions and shallow groundwater, creating conditions conducive to dolomite formation, especially in arid and semi-arid environments where dolocrete commonly forms (14, 70). The interplay between temperature and evapotranspiration influences the kinetics of dolomite precipitation, with higher temperatures generally increasing the rate of formation (69). In some cases, dolomite precipitation can occur in environments exposed to seasonally wet conditions with significant siliciclastic input (like tephra), suggesting that the interaction between wet and dry periods, influenced by temperature and evapotranspiration cycles, can create favourable conditions for dolomite precipitation and dolocrete formation (53). Varying concentrations of dolomite in tephra and hardpan layers at Jwalapuram highlight fluctuations in evapotranspiration and temperature. The correlation matrix shows a strong positive relationship with Loss on Ignition (LOI) based carbonate (%).

The LOI method is a valuable tool for estimating the carbonate content in tephra deposits, which can provide insights into past temperature and evapotranspiration changes(71). By heating samples to around 950°C, LOI measures the inorganic carbon content, which is directly proportional to the carbonate percentage(72). In tephra deposits, higher carbonate content can indicate periods of increased evaporation and lower precipitation, as these conditions promote the concentration and precipitation of carbonate minerals. Conversely, lower carbonate content may suggest cooler, wetter conditions with reduced evapotranspiration. This relationship allows researchers to infer past climatic conditions from tephra layers, offering a proxy for understanding past environmental changes, particularly in volcanic regions where tephra deposits are prevalent(12, 53).

4.4 Palaeovegetation and $p\text{CO}_2$ proxies

$\delta^{13}\text{C}_{\text{SOM}}$: The carbon isotope composition of soil organic matter ($\delta^{13}\text{C}_{\text{SOM}}$) is influenced by a complex interplay of environmental and biological factors. These fluctuations are primarily driven by changes in atmospheric CO_2 composition ($\delta^{13}\text{C}_{\text{air}}$), vegetation dynamics, and soil microbial activity(73–76). This method is based on the principle that C_3 and C_4 plants have distinct carbon isotope signatures, which are preserved in soil organic matter over geological timescales(76, 77). By analysing $\delta^{13}\text{C}_{\text{SOM}}$ values in palaeosols, researchers can estimate the relative abundance of C_3 and C_4 plants in past ecosystems, providing insights into palaeoclimate conditions and vegetation shifts(76, 78). Additionally, because plant $\delta^{13}\text{C}$ values are influenced by atmospheric CO_2 concentrations, $\delta^{13}\text{C}_{\text{SOM}}$ can be used to infer past $p\text{CO}_2$ levels, particularly when combined with other proxies(79, 80).

$\delta^{13}\text{C}_{\text{SOM}}$ values of tephra and hardpan layers at Jwalapuram show a sinusoidal pattern that could be related to seasonal or annual shifts in plant growth patterns, particularly the relative abundance of C_3 versus C_4 plants, contributing significantly to $\delta^{13}\text{C}_{\text{SOM}}$ variability(76).

Additionally, temperature and moisture fluctuations affect microbial decomposition rates and fractionation processes in the soil, further modulating $\delta^{13}\text{C}_{\text{SOM}}$ values(81). The input of fresh organic matter from plant litter and root exudates, which varies seasonally, also plays a crucial role in altering the overall $\delta^{13}\text{C}_{\text{SOM}}$ signature. These seasonal changes in $\delta^{13}\text{C}_{\text{SOM}}$ reflect the dynamic nature of carbon cycling in ecosystems and provide valuable insights into plant-soil-atmosphere interactions, making $\delta^{13}\text{C}_{\text{SOM}}$ an important proxy for understanding both modern and palaeoenvironmental conditions. However, it is important to note that factors such as soil decomposition processes and diagenesis can alter $\delta^{13}\text{C}_{\text{SOM}}$ values, potentially biasing palaeovegetation reconstructions(82). At Jwalapuram, $\delta^{13}\text{C}_{\text{SOM}}$ is strongly correlated with other proxies related to chemical weathering, precipitation, and temperature.

5: Palaeoclimate observations

Our current study draws upon the extensive geoarchaeological, geomorphological, and sedimentological datasets previously gathered from the Jwalapuram area. By integrating these older sedimentological data(1, 3, 4, 6, 8) with new geochemical analyses, we present a comprehensive multi-proxy synthesis of the deposition and reworking processes of the Youngest Toba Tuff (YTT) in the Jurreru basin. This analysis includes magnetic susceptibility measurements, granulometric analyses, loss on ignition (LOI), and other geochemical studies of tephra and hardpan samples from sites JWP3 and JWP2020 (see table S4 for synthesis).

5.1 Sedimentological Dataset

The accumulation of volcanic tephra at Jwalapuram is attributed to multiple episodic deposition events, with at least six to seven distinct depositional episodes identified. The primary air-fall ash layer, approximately 5 cm thick at the base of unit C1, marks the initial stage of deposition (figs. S2 and S4). This layer is followed by subsequent periods of tephra redeposition, where each hardpan layer signifies the end of a redeposition event. Each combination of a YTT unit

and its capping hardpan represents a single depositional cycle, likely corresponding to annual monsoons (fig. S2 and S17).

Particle distribution analysis (PDA): Hardpans can be texturally defined as silt or silt loam, while tephra samples are predominantly silt loam. Sequential granulometric analysis of the tephra deposit across layer C shows overall grain size consistency, highlighting the relative purity of the YTT deposit (fig. S18)(3). The primary air-fall ash layer possesses a higher proportion of finer grains compared to the overlying tephra deposit samples. Most of the hardpans are composed of finer particles than the tephra layer, primarily due to the cementation of the upper finer portion of tephra units. This fining-upward sequence is common in all six tephra units (fig. S6), suggesting fluvial sorting of ash and supporting the argument of ash redeposition in an aqueous medium (figs. S4 and S6)(3, 4, 6, 7).

Magnetic susceptibility: The magnetic susceptibility of the tephra (mean of $42.5 \times 10^{-8} \text{ m}^3 \text{ kg}^{-1}$) is relatively low compared to hardpans and other litho-units (fig. S18). The rhyolitic Toba ash, predominantly composed of diamagnetic SiO_2 (quartz), has low magnetic susceptibility⁷⁹. The presence of Fe-Ti oxides in the ash likely contributes to its magnetic susceptibility. However, any increase in magnetic susceptibility can be attributed to the increased input of material other than volcanic glass, likely from biogenic sources. All hardpans show an increase in magnetic susceptibility, primarily due to higher concentrations of fine grains containing Fe-Ti oxides². Alternatively, the magnetic properties of the hardpans may result from biogenic processes, such as the formation of secondary magnetic minerals by bacterial magnetosomes(83, 84). Past bacterial activity may also cause the dark grey staining and speckled patterns seen on some hardpan surfaces (fig. S12), alongside the possible formation of MnO_2 under weathering and/or oxidizing conditions(61).

Carbonate (%): The volcanic ash strata possess relatively low carbonate contents, ranging from 1.2% to 6.4%, with the highest value in the uppermost tephra unit (unit C6; fig. S18). In contrast, the hardpans exhibit very high carbonate values (6.6% to 28%), which gradually increase with successive hardpan layers until the occurrence of the ashy sand layer (layer B)(3). This trend complements the LOI and dolomite (%) concentration data from JWP2020, showing a stepwise increase in dolomite concentration in subsequent hardpan layers. Silica and dolomite, precipitating at the contact between different phases of redeposition, may also contribute to the consolidation of these hardpans. The presence of mud cracks in the volcanic ash supports desiccation episodes associated with hardpan formation (fig. S15)(3). Periods of aridity after the Toba eruption could have resulted in the precipitation of carbonate (dolomite) and silicate minerals, creating a hardpan layer(10).

5.2 Geochemical Dataset

Chemical weathering of tephra

Principal Component Analysis of elemental (ED-XRF), mineralogical (XRPD), and molecular (ATR-FTIR) data shows negligible variation in the geochemical composition of Toba tephra from all six units highlighting its relative purity and suggesting no mixing with non-tephra material, something likely facilitated by rapid mobilisation and deposition of tephra in the Jurreru basin (figs. 3 and S24)(3, 4). However, we observe notable geochemical differences between tephra and hardpan layers which has significant palaeoclimatic implications. It was observed that all tephra layers contain a higher concentration of immobile elements and silicate minerals. In contrast, the hardpan layers show relatively lower concentrations of immobile elements and silicate minerals. The hardpans contain higher concentrations of base and other mobile elements, which are quite low in all tephra units. Stepwise increase in the concentration of mobile elements in hardpan layers highlights an increasing intensity of chemical

weathering(53, 85). A similar trend is observed in $\Sigma_{\text{Bases}}/\text{Al}_2\text{O}_3$ and $\Sigma_{\text{Bases}}/\text{TiO}_2$ values, demonstrating increasing hydrolysis and leaching of tephra-derived silicate minerals (fig. S23). It is inversely reflected in other weathering proxies like $-f_{\text{diss}}$, CIA, CIW, and PIA that highlight the increasing aggregation of weathering elements³¹. A notable fall in the concentration of feldspar and biotite in the hardpan layers in comparison to the tephra layers strongly correlates with $-f_{\text{diss}}$ and increasing concentration of dolomite.

Palaeoprecipitation

Here we use Rb/Sr ratio as proxy to infer palaeoprecipitation in the tephra unit of Jwalapuram. The Rb/Sr value of tephra samples is higher in comparison to hardpans, indicating a wetter environment during tephra deposition and drier environment during hardpan formation. Fluctuation in Rb/Sr ratios reflects notable changes in the concentration of Sr across the YTT unit. Sr tends to leach from tephra during hydrolysis and precipitates along with base elements due to warming periods(13, 53). We observed a sinusoidal pattern in Rb/Sr values, likely reflecting wet and dry cycle, representing monsoonal cyclicality. There is notable decrease in Rb/Sr values in upper hardpan layers (C3 – C5), likely related to the weakening of precipitation in the area which shows strong correlation with increasing carbonate (%), concentration of mobile elements, and dolomite.

Palaeotemperature and evapotranspiration

Evaporites such as dolomite or calcite are highly sensitive to changing evaporative and temperature conditions. Step-increases in the concentration of dolomite in successive hardpan layers coincide with increases in the concentration of base elements and carbonate (%). We interpret this as a sign of increasing evaporative conditions and surface warming(10, 12, 53, 68–70). Decreasing Rb/Sr values of hardpan indicate the same, suggesting a decrease in precipitation and increase in aridity. It is also important to note that the topmost unit of tephra

(C6) lacks hardpan and shows a drastic decrease in dolomite concentration and carbonate (%), suggesting a lowering of temperature and decline in evapotranspiration.

Palaeovegetation

Like palaeoprecipitation and palaeotemperature proxies, we observe a sinusoidal trend in $\delta^{13}\text{C}_{\text{SOM}}$ values of tephra deposit samples at Jwalapuram, showing mixed vegetation signatures with certain proportional variation across the tephra sequence. All tephra layers show a decrease in $\delta^{13}\text{C}_{\text{SOM}}$ values relative to hardpan layers, likely indicating a shift towards a C_3 dominated environment. Conversely, we observe positive excursions in $\delta^{13}\text{C}_{\text{SOM}}$ values during hardpan formation suggesting relatively dry and C_4 inclined conditions(76, 86). However, the annual variation in $\delta^{13}\text{C}_{\text{SOM}}$ values might relate to fluctuation in $p\text{CO}_2$ which directly impact surface vegetation(80). The correlation matrix shows a strong correlation between $\delta^{13}\text{C}_{\text{SOM}}$ and other chemical weathering proxies. Earlier works have demonstrated strong positive relationship with silicate weathering(38, 40, 41).

6: Correlating YTT, ENSO, and ISM: Probable reason behind surface warming

The intricate interplay between El Niño Southern Oscillation (ENSO), Indian Summer Monsoon (ISM), Indian Ocean Dipole (IOD), and tropical volcanic eruptions can lead to significant climate anomalies, including monsoon failures and temperature changes(87–90). A prime example is the 2002 Indian monsoon failure, where an El Niño event weakened the typical monsoon circulation, resulting in a 19% rainfall deficit across India(85, 91). This occurred despite a simultaneous positive IOD event, which usually enhances monsoon rainfall, demonstrating the complex nature of these teleconnections(87). Another illustrative case is the aftermath of the 1991 Mount Pinatubo eruption in the Philippines. While volcanic eruptions generally cause short-term global cooling, the Pinatubo eruption altered the ENSO-monsoon relationship, affecting temperature and precipitation patterns across the Indian subcontinent

(fig. S34)(92). These examples underscore the intricate relationships between these climate phenomena and highlight the challenges in predicting monsoon behaviour and temperature patterns(89, 92). The varying influences of ENSO, IOD, and volcanic activity on the ISM demonstrate the complexity of Earth's climate system and the need for comprehensive understanding of these teleconnections to improve climate forecasting and preparedness for extreme weather events(87, 92).

We argue that the gradual increase in concentration of dolomite and leaching of base cations suggest gradual warming of the environment after the YTT eruption. We interpret this warming trend as an indicator of an El Niño phase influenced by a YTT event lasting for 3 – 4 years. Here we present such example of temperature rise and weakening of the Indian monsoon in the studied region (i.e. Andhra Pradesh) after the 1991 Mt. Pinatubo eruption(92, 93). The annual mean temperature of India dropped by 0.13°C during 1992 (based on IMD dataset). Rainfall anomaly data of Andhra Pradesh show a drastic fall in rainfall volume indicating weakening of the ISM after the Pinatubo eruption. This El Niño phase lasted for 4 years and peaked in 1995, resulting into severe drought conditions during 1992-1995. Severe meteorological drought was observed in humid subtropical zones of N. India during this phase(94). We suggest that the YTT may have induced similar or more severe conditions.

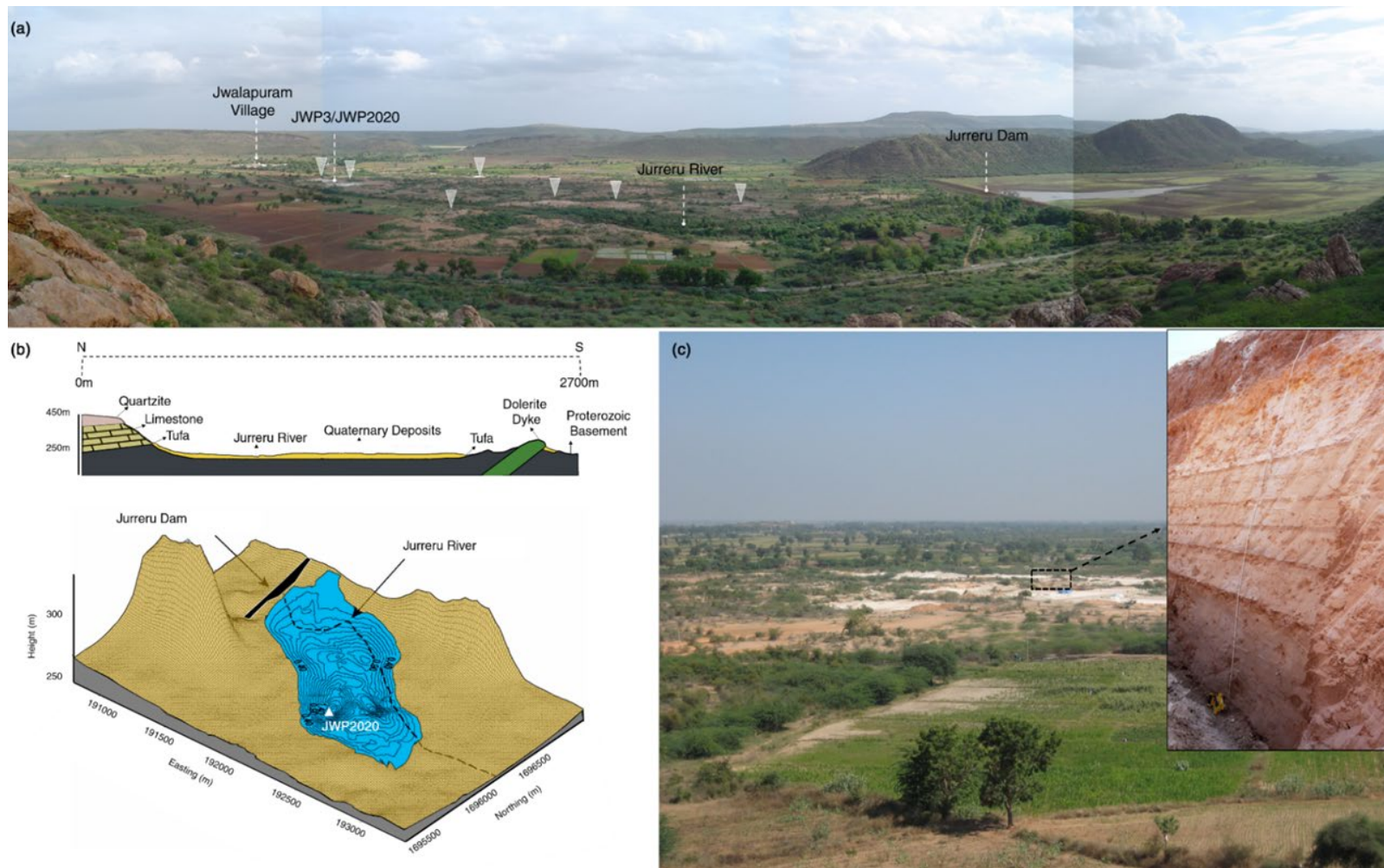


Fig. S1. (a) Landscape view of the Jurreru valley near Jwalapuram, highlighting the location of JWP3/JWP2020 locality, Jwalapuram village, Jurreru river, and Jurreru dam. White triangle points towards the exposed YTT deposits; (b) Elevation profile (top) of the region showing major lithological features and digital elevation model of the region (base); DEM shows that the locality of JWP2020/JWP3 is lowest topographical point in the area; It may have acted as a sediment trap which explains the thick deposits of YTT in this particular area. Adapted from Blinkhorn et al.⁵ and Petraglia et al.¹; (c) Extensive modern tephra mining at the site, resulting in the exposure of the stratified archaeology yielding YTT sequence with archaeology above the ash. Picture credit: (a and c) Kadapa District Archaeology Project (KDAP).

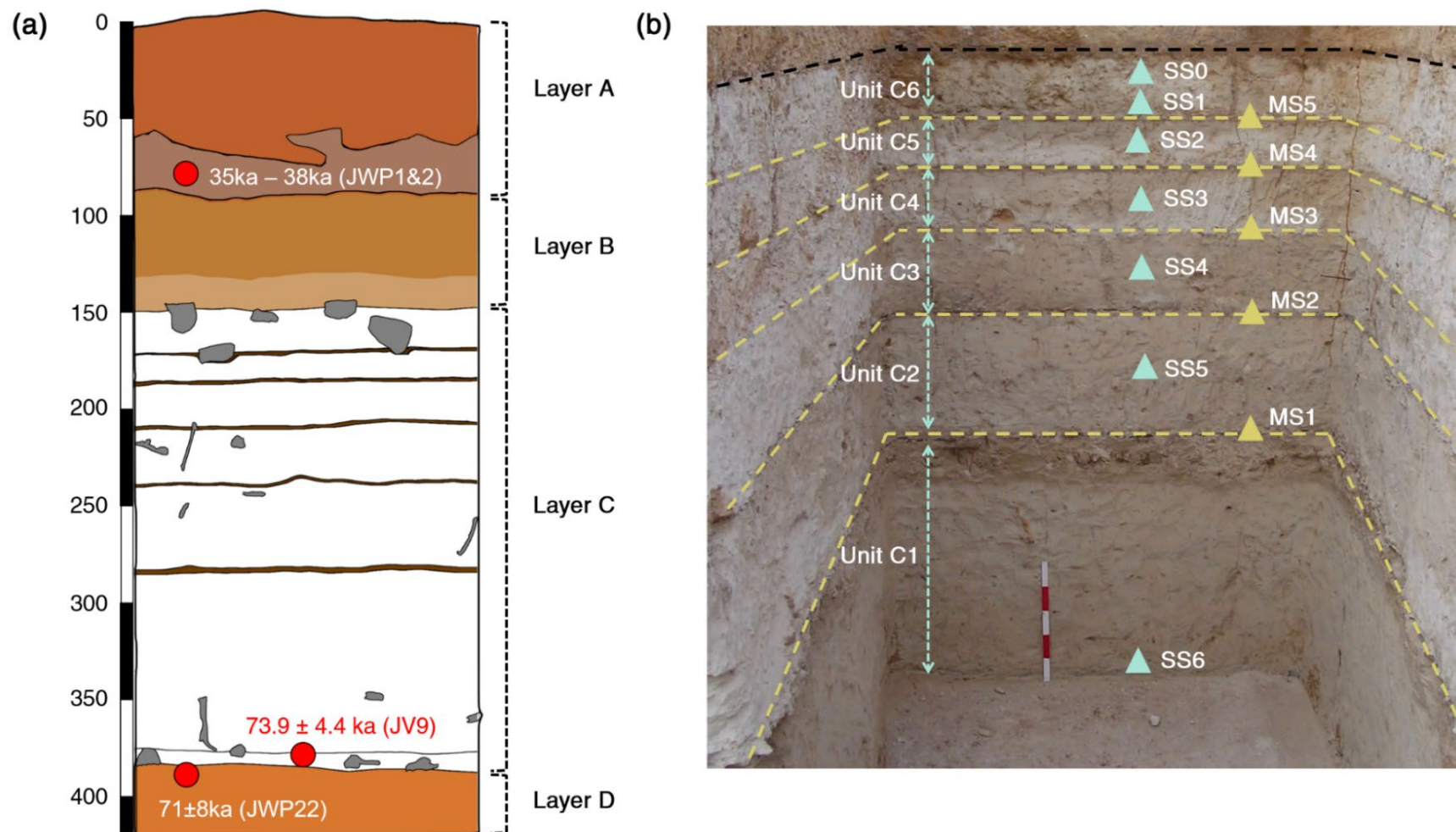


Fig. S2. (a) Lithostratigraphy of JWP3, comprised of four layers (A-D) where Layer A and Layer D contain Middle Palaeolithic lithic assemblages; (b) YTT containing Layer C comprises of six sub-units representing six episodes of Toba ash deposition, demarcated by five hardpan layers (mustard line). Current work solely focusses on the unit – C and its sub-units. Two samples were collected from each unit: tephra (aqua blue) and hardpan (mustard). Note: JWP3 and JWP2020 has a mirroring stratigraphy. Source: (b) picture is taken from KDAP project. Picture credit: (b) Kadapa District Archaeology Project (KDAP).

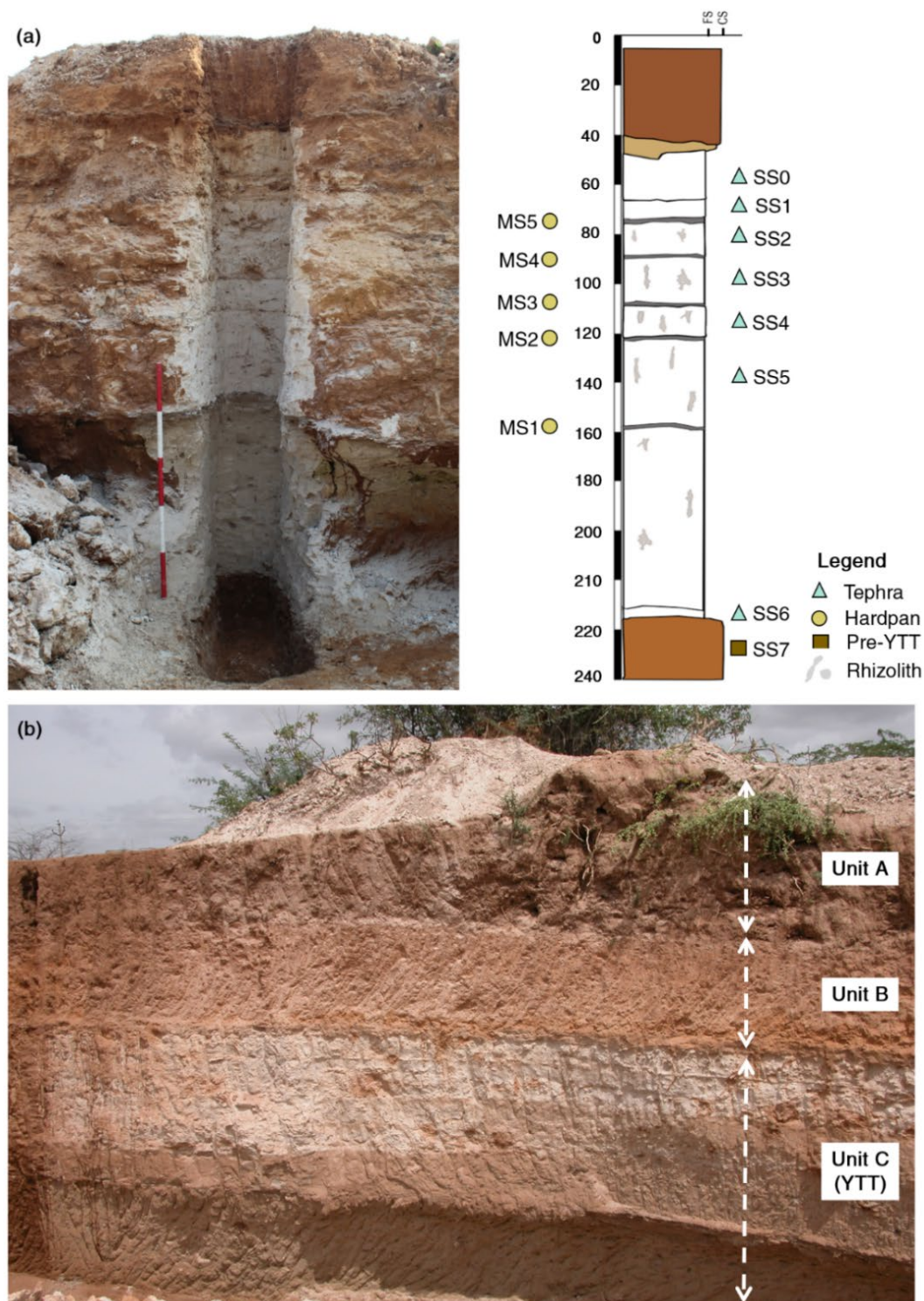


Fig. S3. (a) Excavated trench of JWP2020 and litho-stratigraphic profile showing location of collected samples; (b) Freshly mined archaeology bearing YTT sequence (80m north to JWP3). All YTT sequences have comparable stratigraphy, mostly situated in a low-lying area with archaeological deposits (fig. S1).

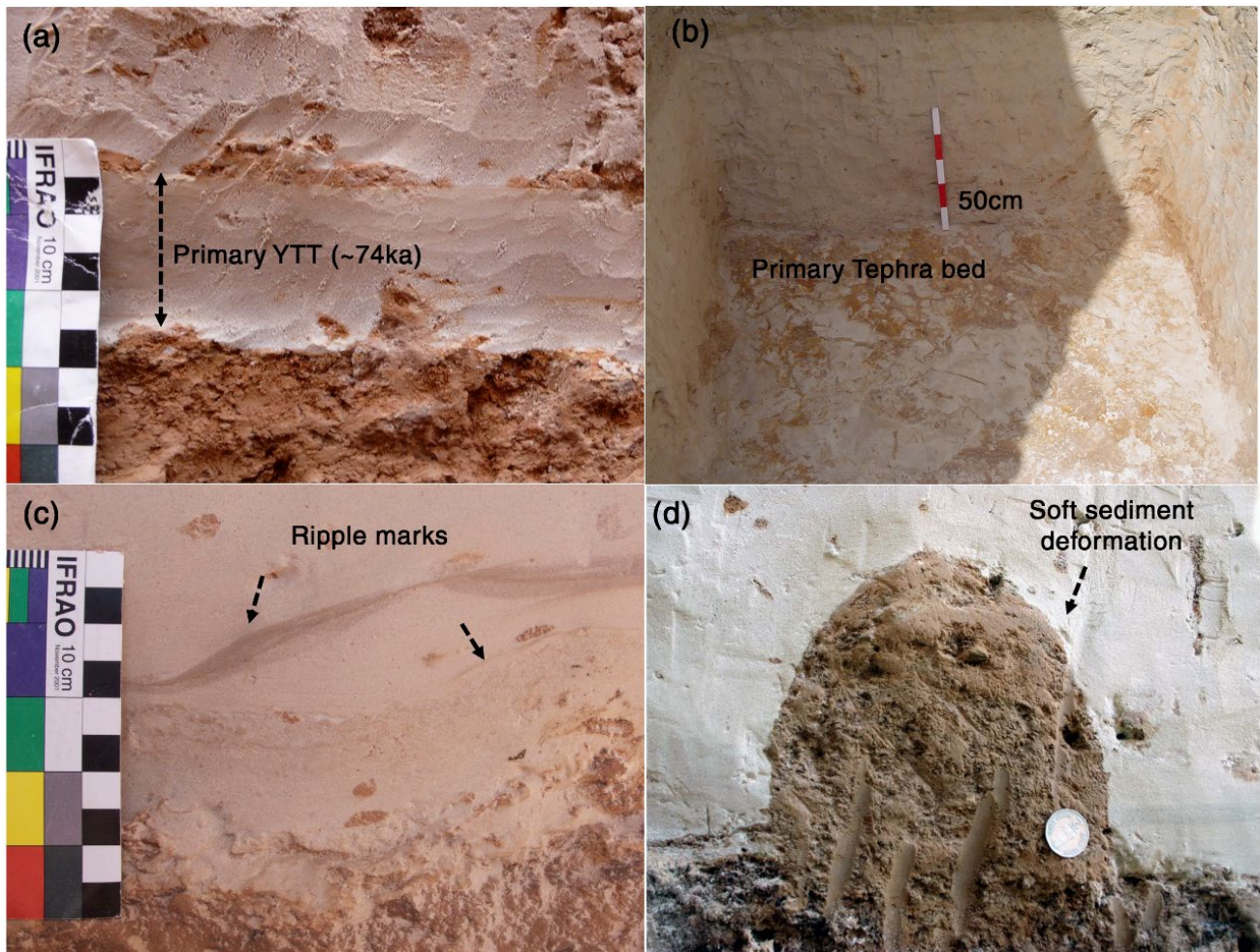


Fig. S4. (a) Basal 5cm of primary air fall YTT tephra demarcated by thin reddish-brown silty sand layer; (b) Superior view of primary YTT bed showing discontinuous layer of reddish-brown silty-sand layer; (c) Prominent ripple and swirling marks were observed in all primary YTT layers, suggesting that the tephra was deposited in an aqueous medium; (d) Presence of soft-sediment deformation at the YTT-layer D interface also suggests the same. Picture credit: Kadapa District Archaeology Project (KDAP).

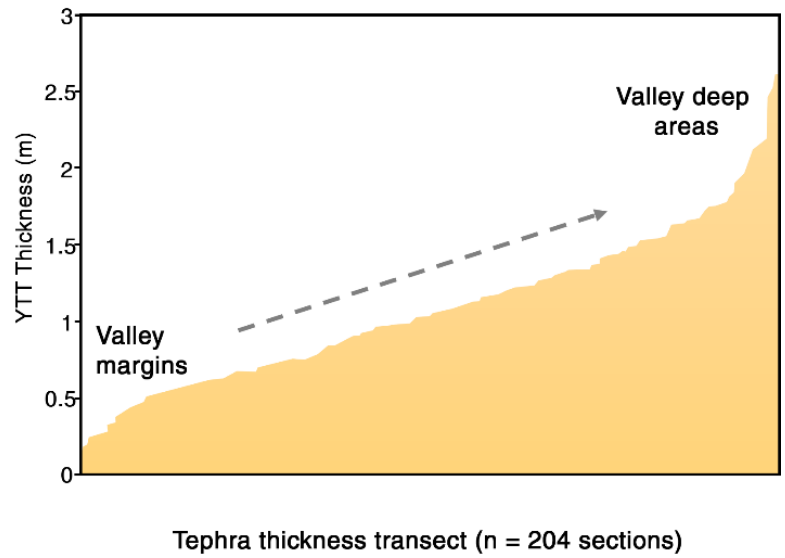
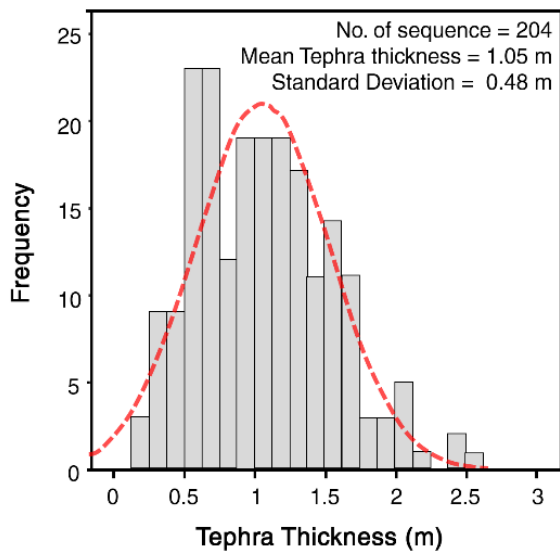


Fig. S5. The plots show variation in the thickness of the YTT deposit across the Jurreru valley near Jwalapuram. Tephra thicknesses vary with changing altitude gradient; thinner at valley margins (e.g., JWP22) and thicker in the central valley (e.g., JWP2020 and JWP3). Both plots are adapted from Jones^{3,7}.

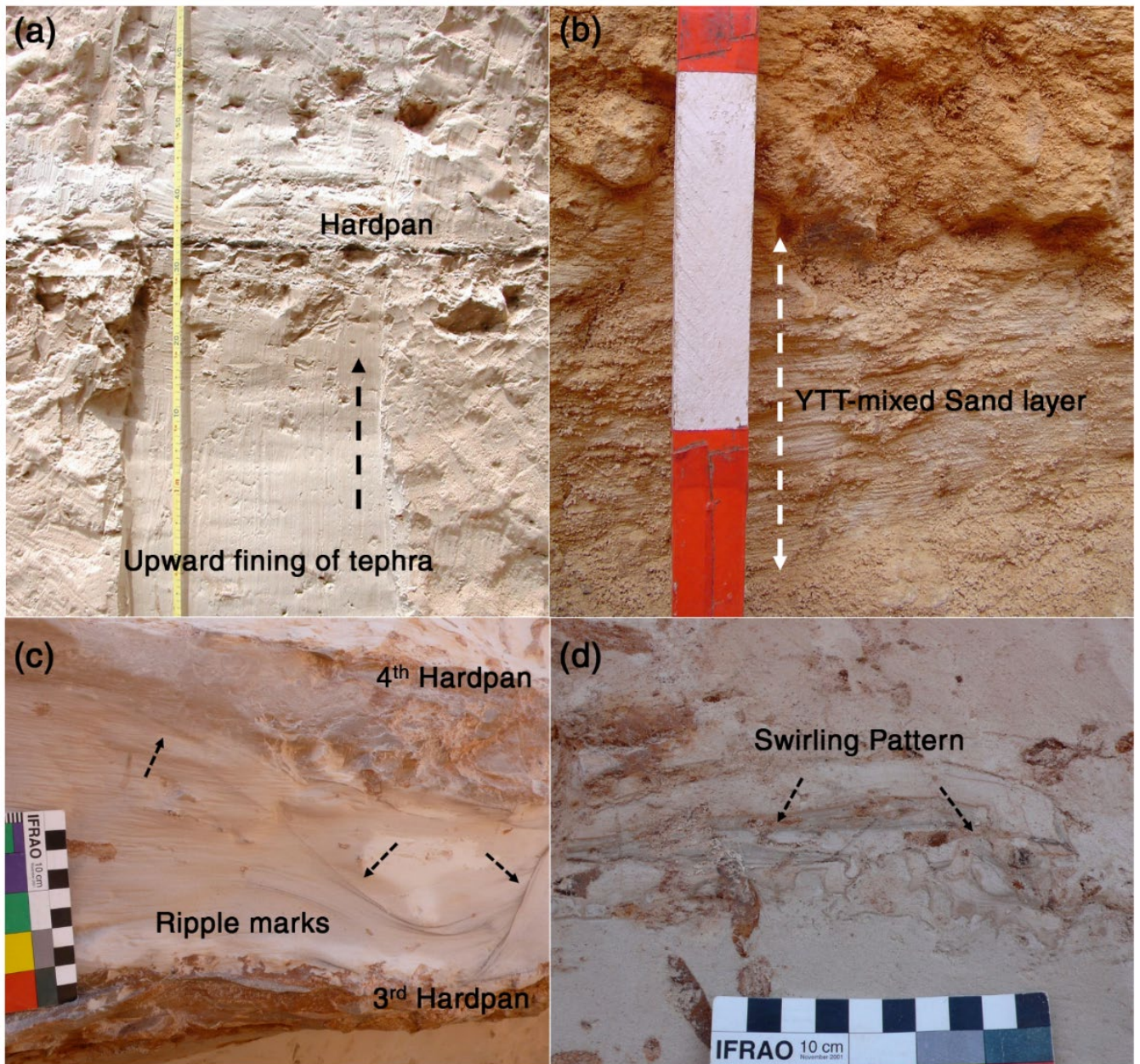


Fig. S6. Multiple stratigraphic features indicate that the all six units (C1 to C6) of Toba ash was deposited in standing water conditions: (a) All tephra units show upward fining of the Toba, likely related to fluvial segregation/sorting; (b) Laminated layer of YTT-mixed sand layer which marks the termination of the YTT deposition phase at Jwalapuram; (c) Like the primary YTT (see fig S5c), all YTT units contain several ripple marks; (d) Swirling pattern observed in most of the YTT units, reinforcing the fact that all YTT unit were deposited in an aqueous setting. Picture credit: Kadapa District Archaeology Project (KDAP).

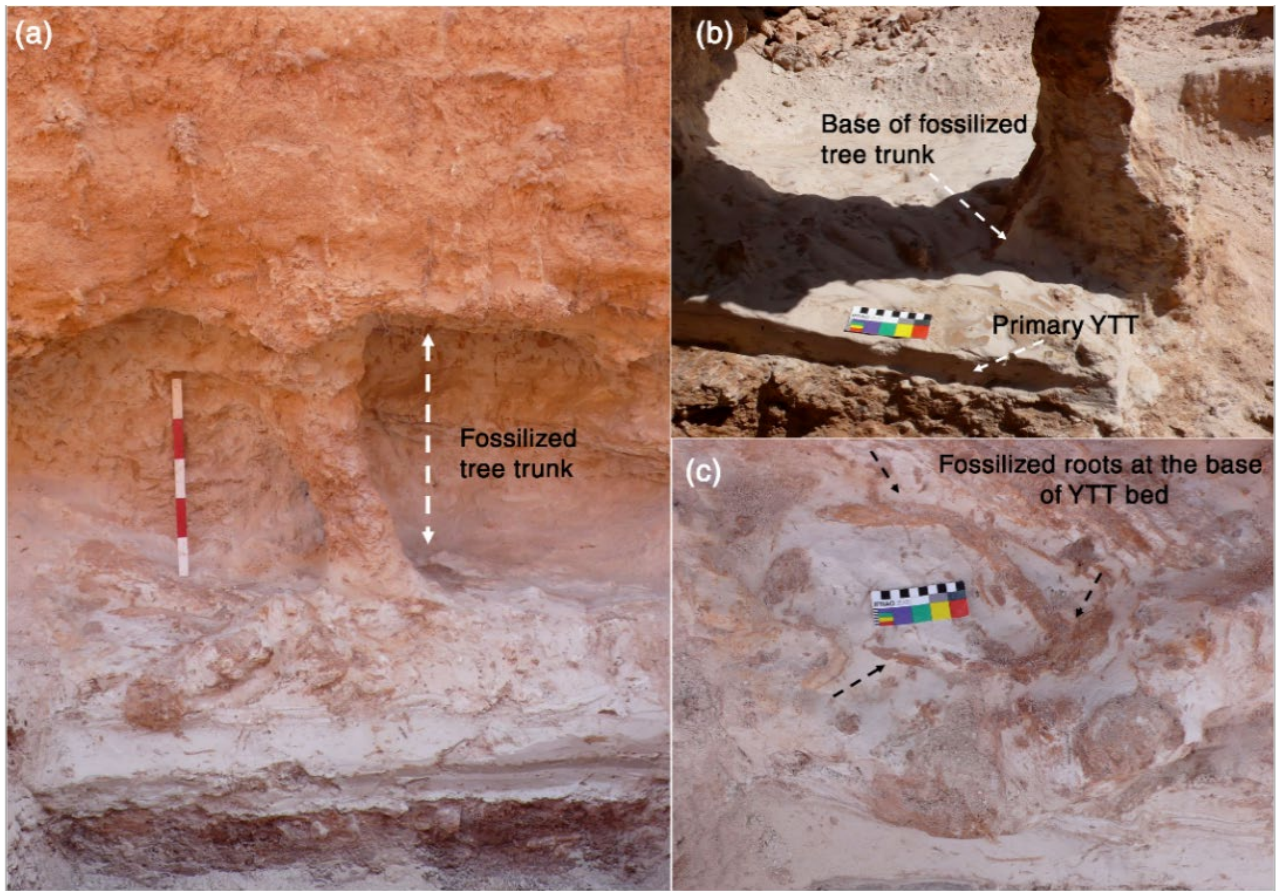


Fig. S7. (a) In-situ fossilized tree trunk buried within the YTT deposit; (b) Multiple fossilized roots were observed at the base of the YTT deposit (layer C), suggesting that the tree was resting on the surface of layer D; (c) Close-up view of fossilized tree roots, as indicated by the black arrow. Exceptional preservation of trees is likely related to their rapid burial by Toba ash. Picture credit: Kadapa District Archaeology Project (KDAP).

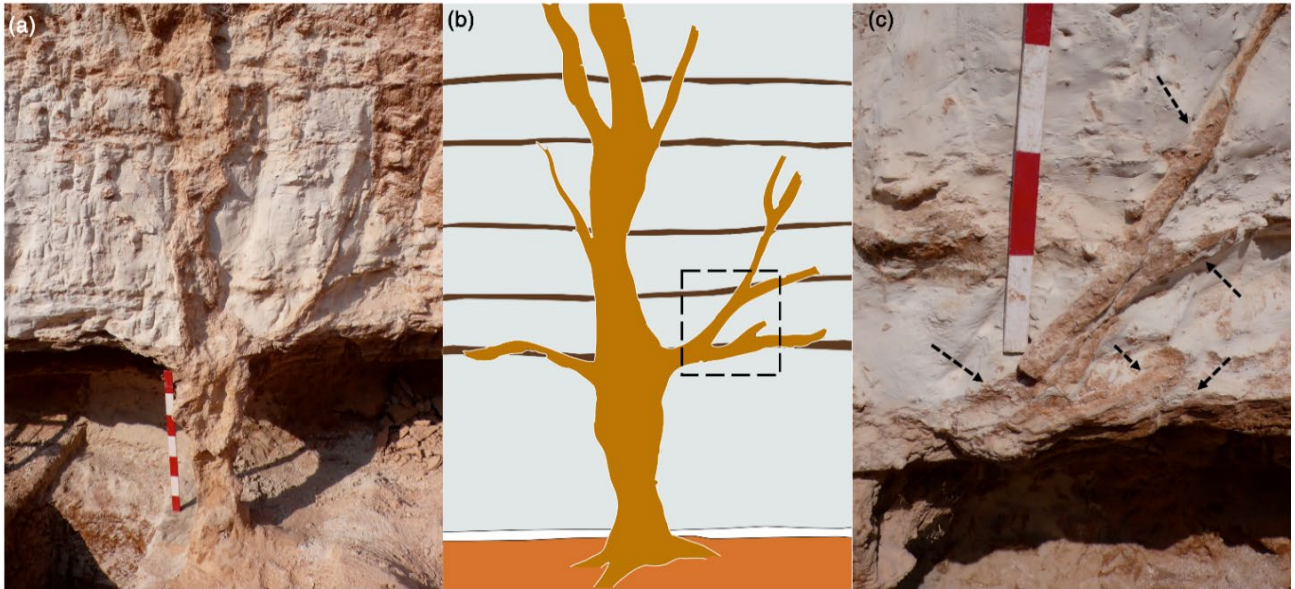


Fig. S8. (a) In-situ fossilized tree trunk embedded in the tephra layer (C); (b) Litholog shows the upright structure of a fossilised tree with branches. Note that tree is resting on a pre-YTT surface and completely buried by the six units of Toba ash; (c) Close-up view of fossilised branches, indicated by the black arrow. Picture credit: Kadapa District Archaeology Project (KDAP).

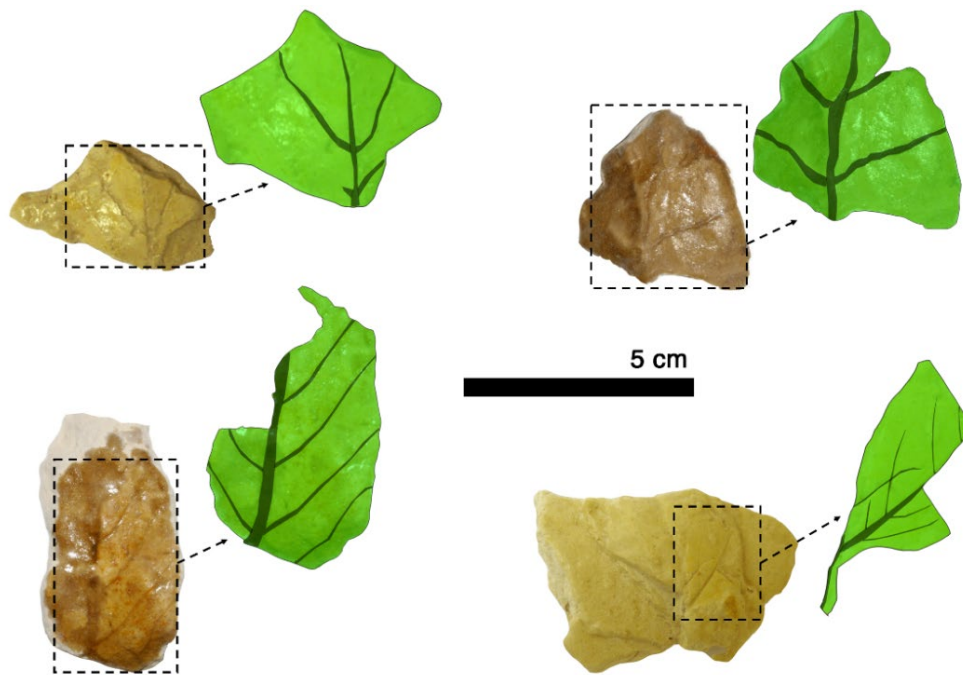


Fig. S9. A large number of fossilized leaf imprints are observed at the boundary between the primary ash fall layer and the first reworked tephra deposits. This deposition of leaves on the primary ash layer suggests a possible defoliation event, which is believed to have been caused by the adverse effects of the ashfall on the trees⁵. Preservation of leaf-casts are facilitated by rapid burial under Toba ash. Picture credit: Kadapa District Archaeology Project (KDAP).

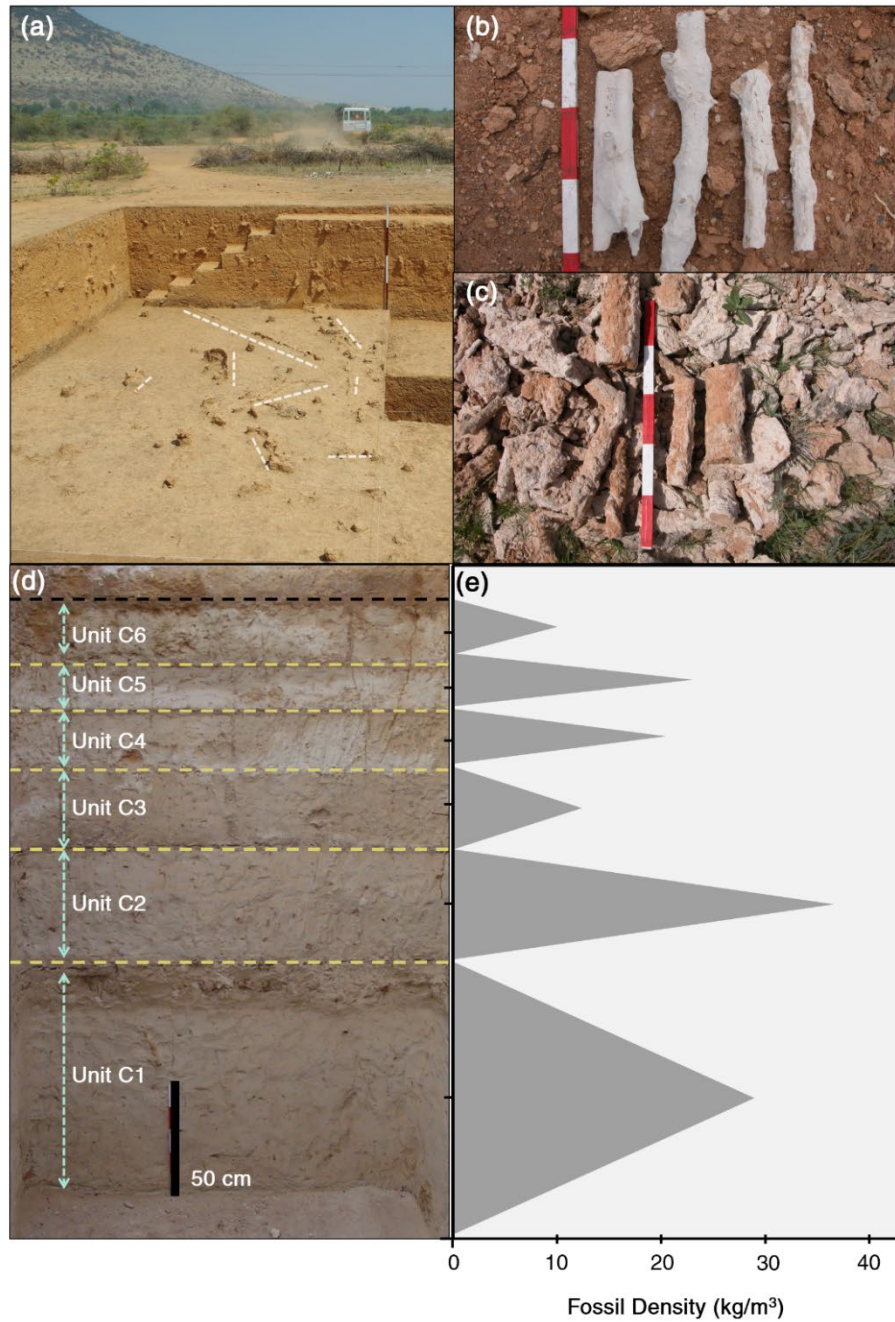


Fig. S10. (a) Dense concentration of rhizoliths (marked by dotted white line) observed in YTT layer of JWP22; (b-c) We observed large dumps of rhizoliths all across the site, as a result of the activity of modern tephra miners; (c-d) Plot shows variation in rhizolith density across the six sub-units of tephra. An exceptionally high density of rhizoliths and tree fossils at the site is the result of the adverse effect of ashfall on local vegetation. Picture credit: Kadapa District Archaeology Project (KDAP).

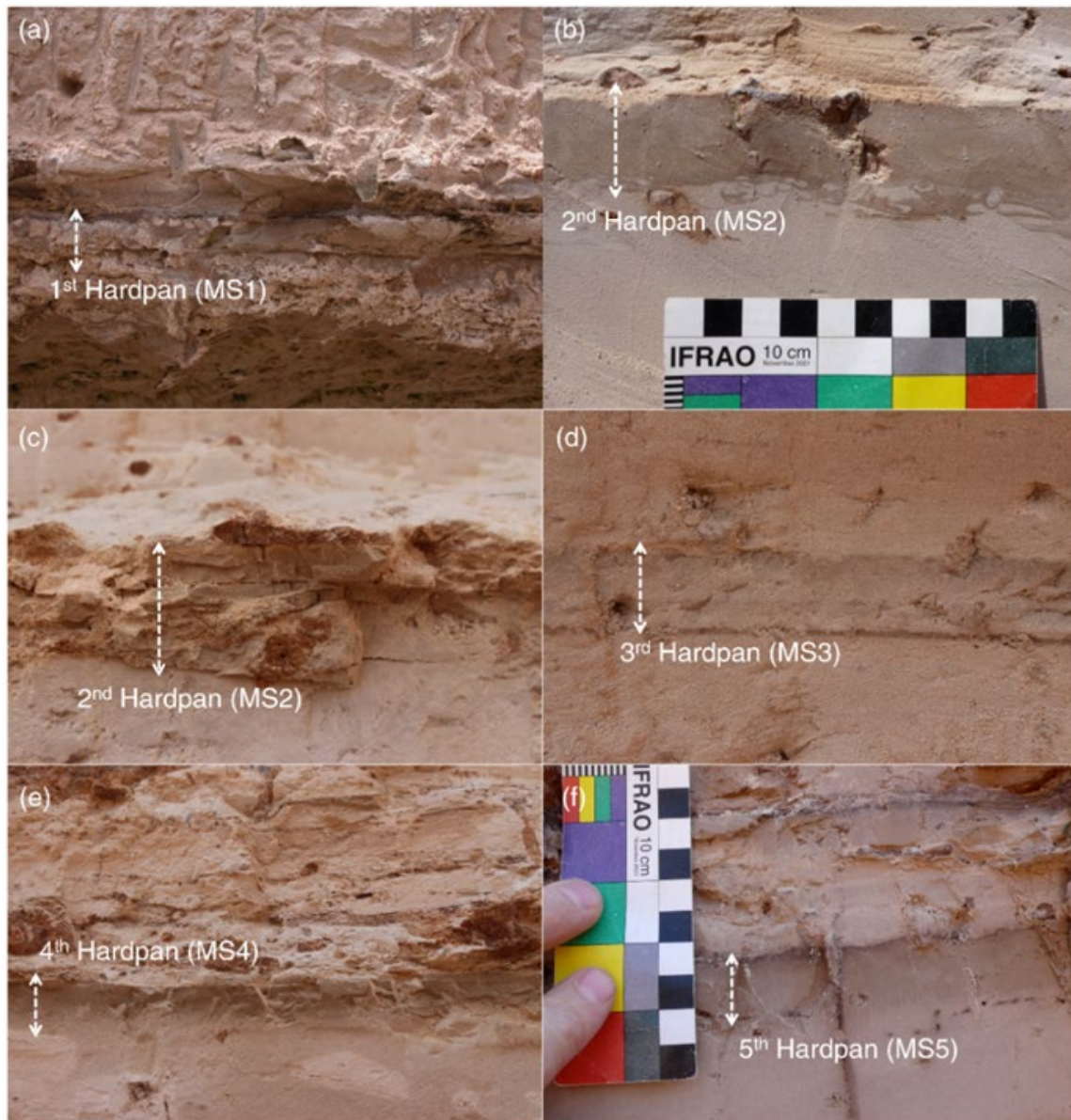


Fig. S11. Close-up view of five brownish-grey hardpan layers demarcating 6 tephra sub-units. (a) first hardpan; (b-c) second hardpan; (d) third hardpan; (e) fourth hardpan; and (f) fifth hardpan. Chemically, most of these hardpans are dolocrete, containing a higher concentration of dolomite.

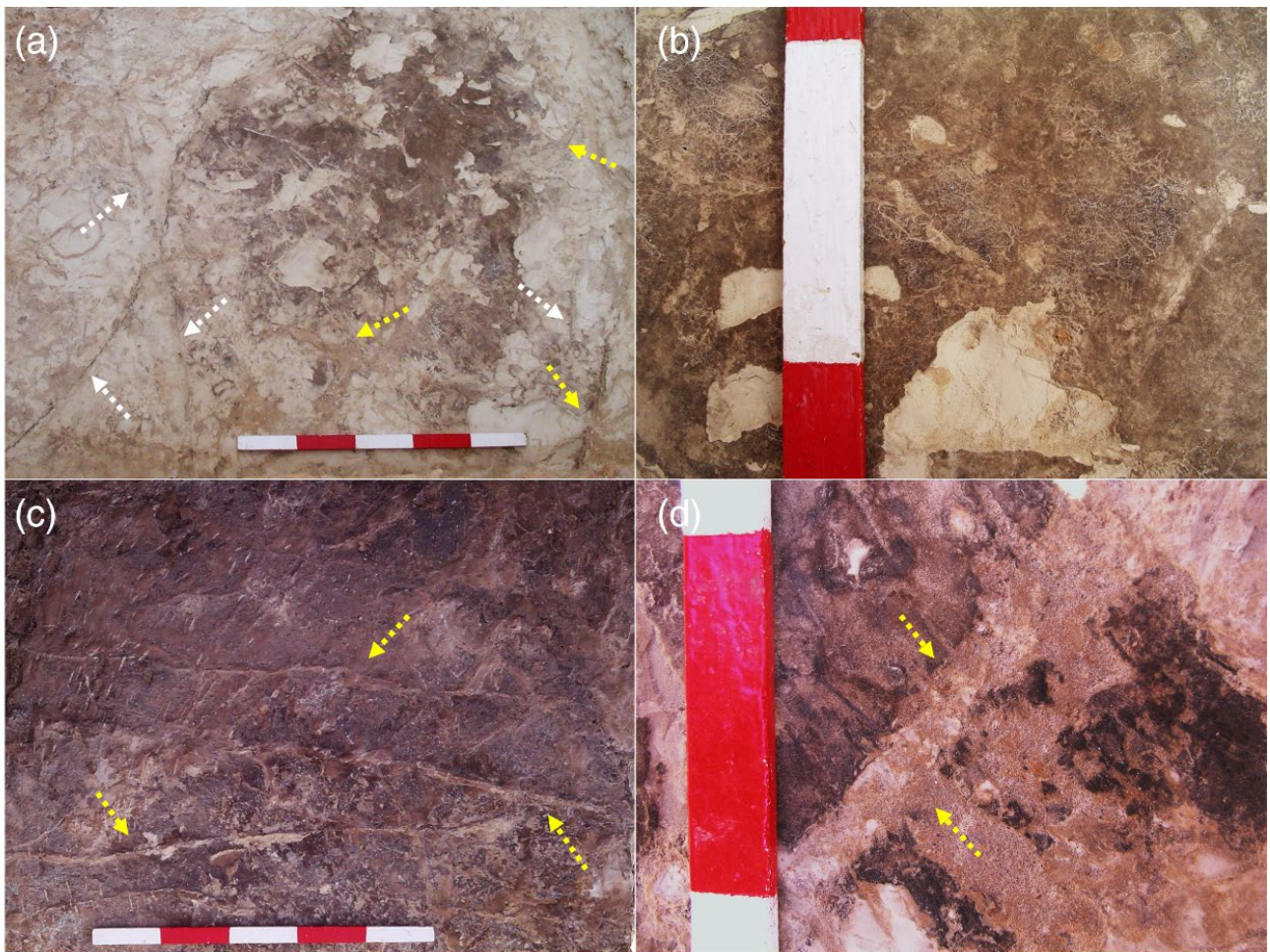


Fig. S12. Superior view of different hardpan layers showing different biogenic features. (a) Presence of mud cracks (pointed by white arrow) are an indicator of tephra desiccation and rapid drying. Yellow arrow indicates toward horizontal root cast and rhizoliths; (b) Multiple rootlet traces; (c) Yellow-arrow showing horizontal rhizoliths; (d) close-up view of one of root cast. Note the black stains all across hardpan surface - these are large microbial-mat surfaces that are strong indicators of desiccation during a dry season. Such mats are a commonly observed feature in the hardpan and duricrust layers. Note: 1 unit of scale = 10 cm. Picture credit: Kadapa District Archaeology Project (KDAP).



Fig. S13. Fragment of Hardpan from Jwalapuram ash quarry. Note the abundance of rhizoliths over hardpan layers. The black stains on the surface of the hardpan is likely a remnant of microbial activity. Picture credit: Kadapa District Archaeology Project (KDAP).



Fig. S14. (a-b) Fossilized burrow networks embedded in the tephra layer (pointed out by black arrow); (c) Burrow tracks and root-tracks on hardpan fragment; (d) Microbial films forming on the top of rootlet-traces, marked by the black Fe-Mn stains. Picture credit: Kadapa District Archaeology Project (KDAP).

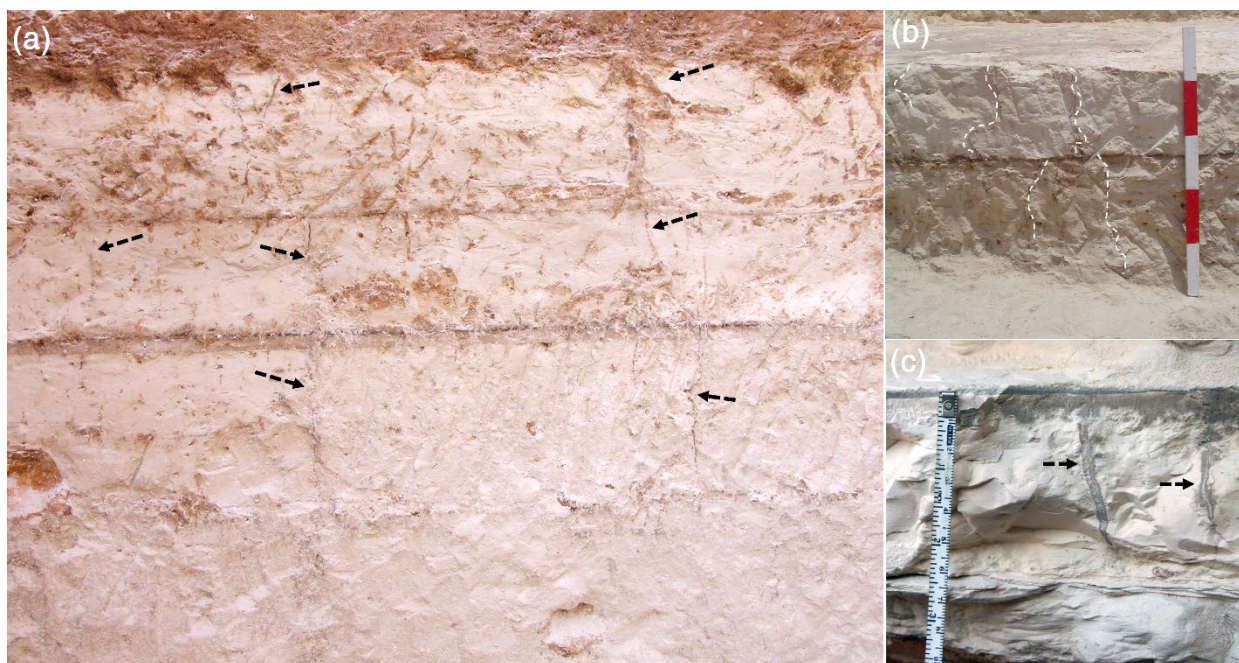


Fig. S15. (a-c) Several mud cracks were observed in all YTT units. These mud cracks are related to the desiccation and wetting-drying of tephra layers. Picture credit: Kadapa District Archaeology Project (KDAP).



Fig. S16. Fossilized termitarium or insect burrow embedded in the Toba tephra layer at Jwalapuram. Picture credit: Kadapa District Archaeology Project (KDAP).

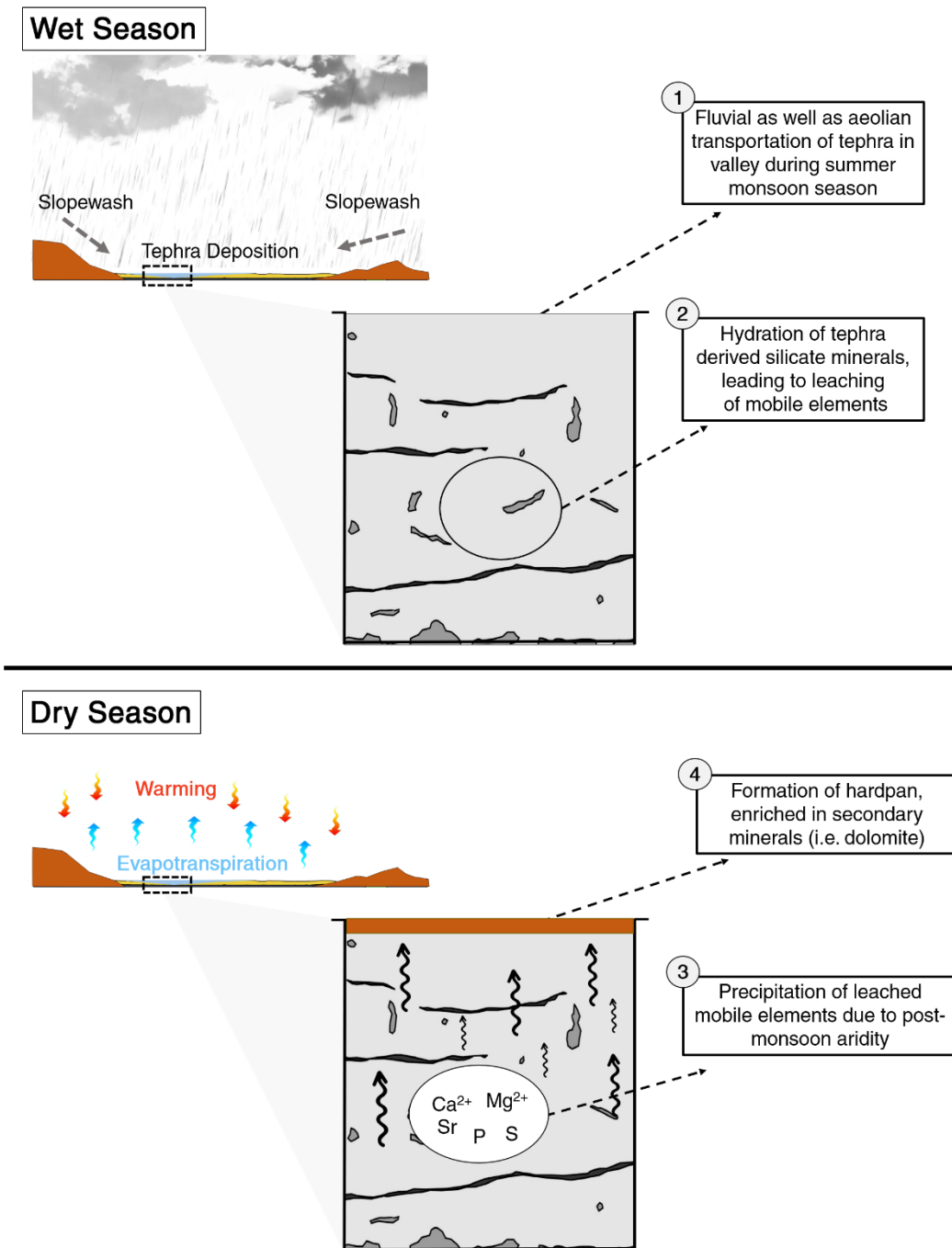


Fig. S17. Reconstruction model based on a multi-proxy geochemical dataset showing monsoonal and post-monsoonal conditions in Jwalapuram after the Youngest Toba Tuff (YTT) event, focusing on the chemical weathering process of volcanic ash and its relationship with seasonality. We observe four distinct stages, starting from tephra accumulation in the basin during the monsoonal season to hardpan formation in the post-monsoonal season. A couplet of a single tephra and a single hardpan layer represents a single monsoonal cycle. Thus, the JWP2020 sequence represents six annual monsoonal cycles after the YTT eruption. The increasing concentration of dolomite suggests strong evaporative conditions, likely related to rising surface temperatures and increasing aridity after each tephra deposition phase.

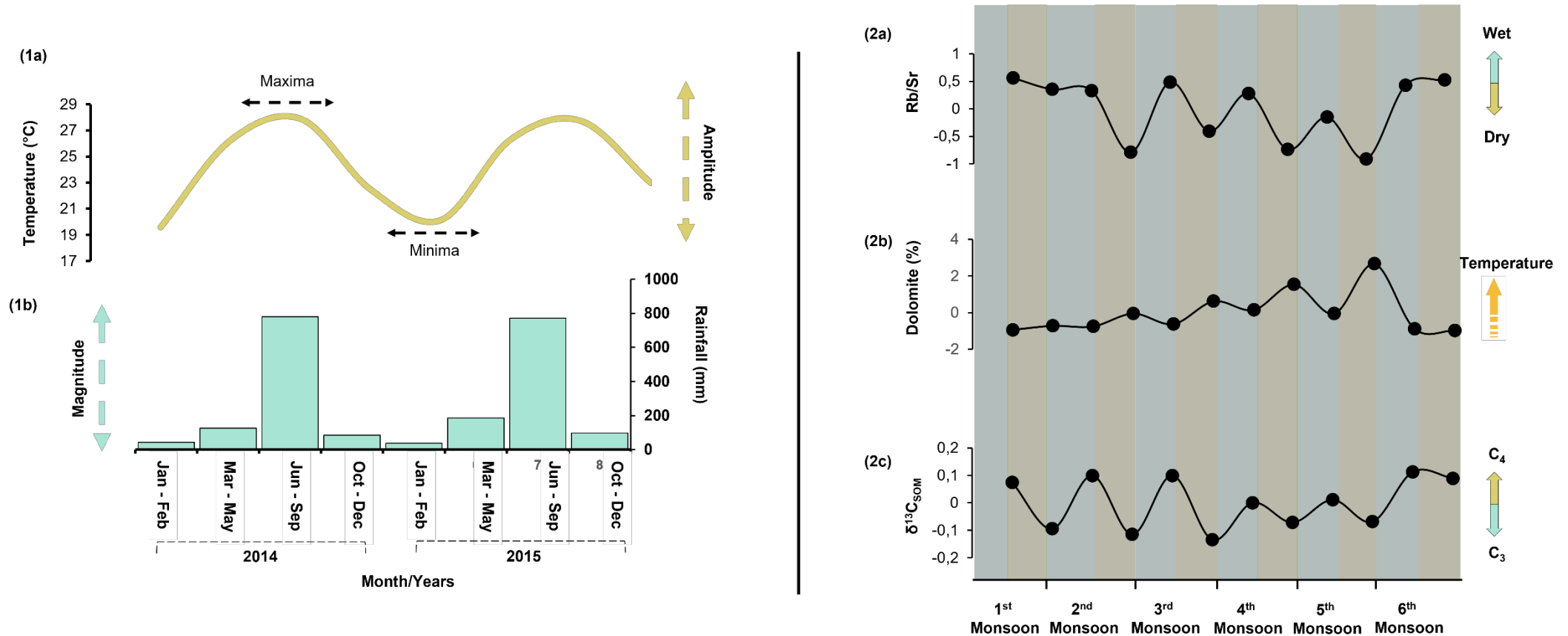


Fig. S18. Climate seasonality reflects oscillatory pattern in temperature and rainfall, defined by its sinusoidal pattern – represented by minima and maxima. Here we use seasonal temperature (1a) and rainfall (1b) data from India (2014-2015) to demonstrate climate seasonality; (2a) Palaeoprecipitation proxy: Rb/Sr; (2b) Proxy for evapotranspiration and temperature – Dolomite; (2c) Palaeovegetation proxy: $\delta^{13}\text{C}_{\text{SOM}}$. We suggest that the distribution pattern observed in the aforementioned proxy data represent seasonality. Note modern climate data is obtained from the Indian Meteorology Department. Legend: aqua blue and mustard bands represent wet and dry seasons respectively.

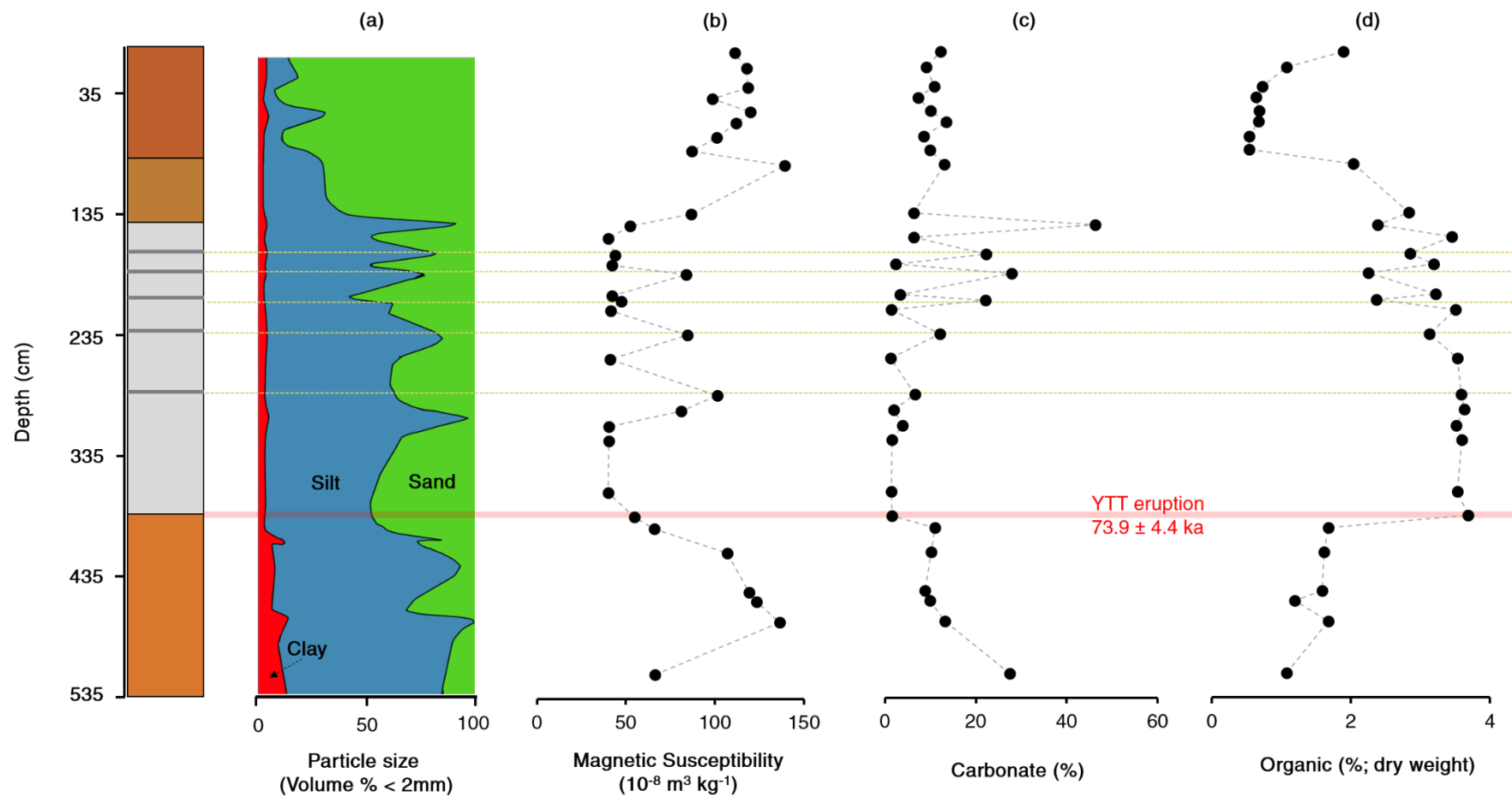


Fig. S19. Geoarchaeological dataset from JWP3: (a) Particle distribution analysis (PDA); (b) Magnetic susceptibility; (c) LOI based carbonate (%); and (d) LOI based organic (%).

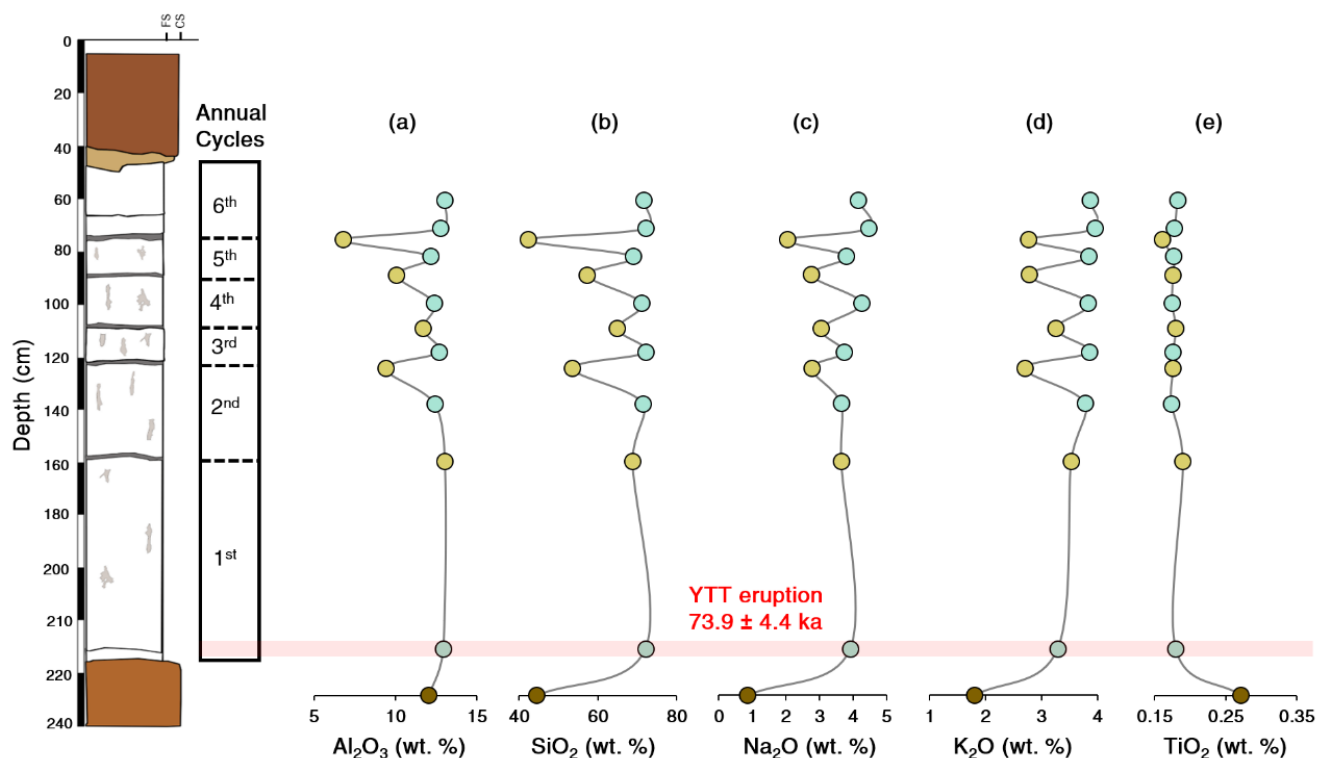


Fig. S20. Concentration of immobile elements across JWP2020 sequence – (a) Al_2O_3 , (b) SiO_2 , (c) Na_2O , (d) K_2O , and (e) TiO_2 . Loss of silicate minerals (i.e. – feldspar and biotite) is positively related to the negative excursions in immobile elements during hardpan layers. Legend: brown: pre-YTT layer, aqua blue: YTT/tephra layers and mustard: hardpan.

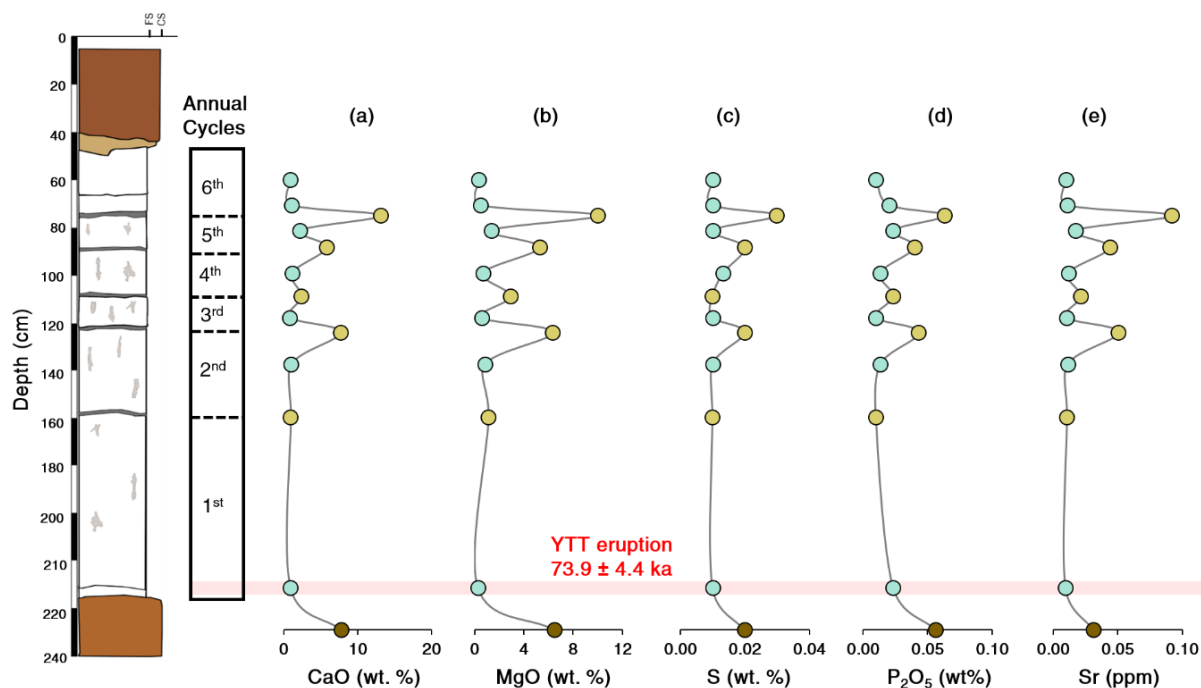


Fig. S21. Concentration of mobile elements across JWP2020 sequence – (a) CaO , (b) MgO , (c) S , (d) P_2O_5 , and (e) Sr . Increasing concentration of dolomite is positively related to the positive excursions in base cations during hardpan layers. Legend: brown: pre-YTT layer, aqua blue: YTT/tephra layers and mustard: hardpan.

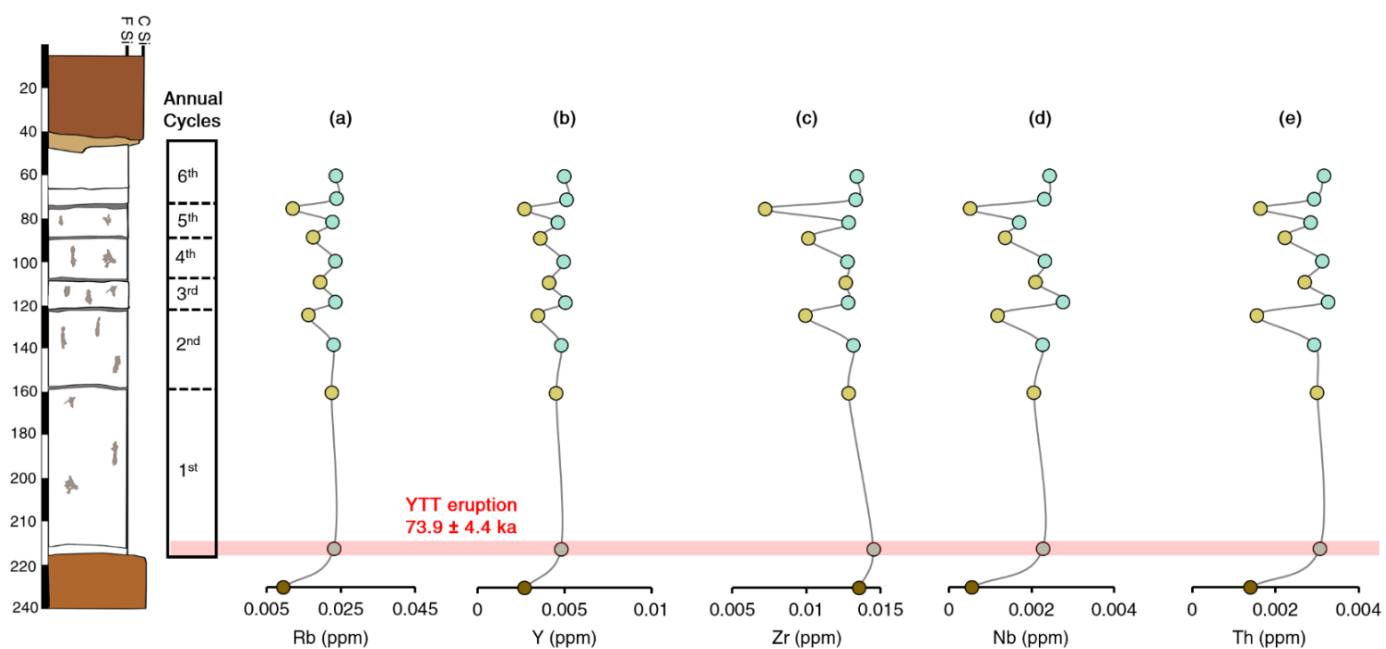


Fig. S22. Concentration of immobile trace elements across JWP2020 – (a) Rb, (b) Y, (c) Zr, (d) Nb, and (e) Th. Legend: brown: pre-YTT layer, aqua blue: YTT/tephra layers and mustard: hardpan.

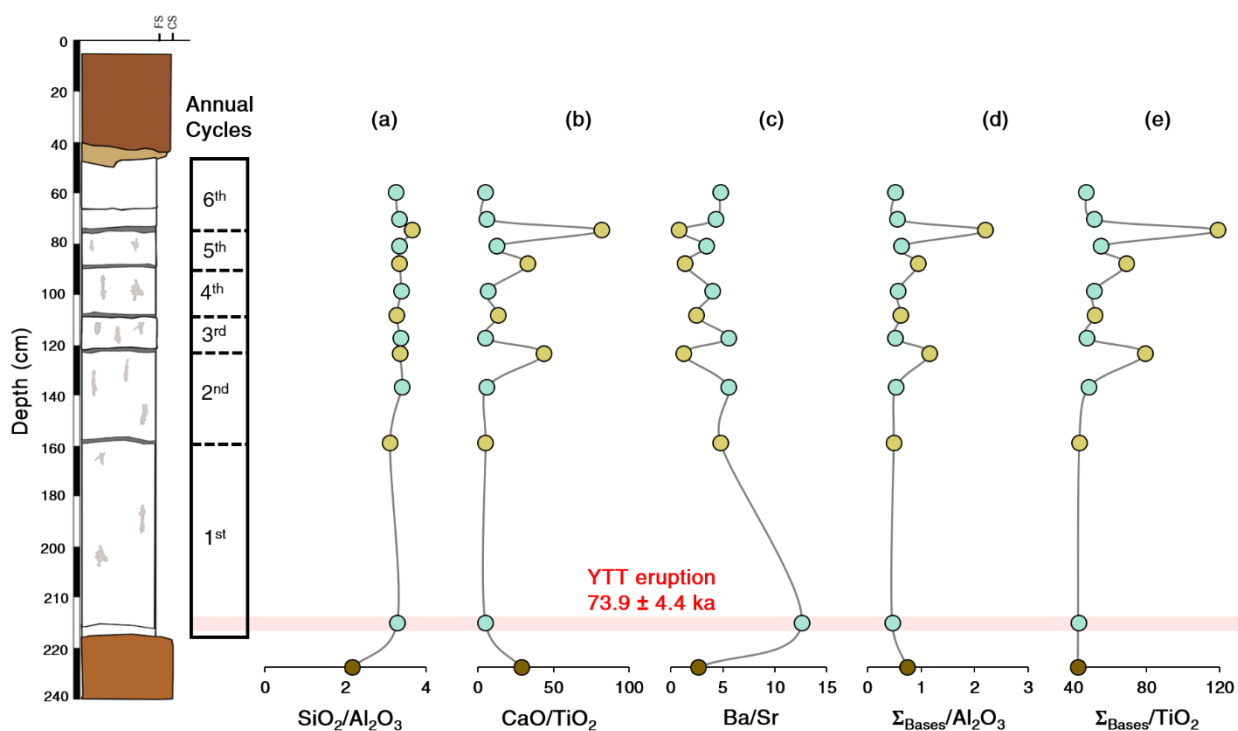


Fig. S23. Elemental ratio - (a) SiO₂/Al₂O₃, (b) CaO/TiO₂, (c) Ba/Sr, (d) ΣBases/Al₂O₃, and (e) ΣBases/TiO₂. Legend: brown: pre-YTT layer, aqua blue: YTT/tephra layers and mustard: hardpan.

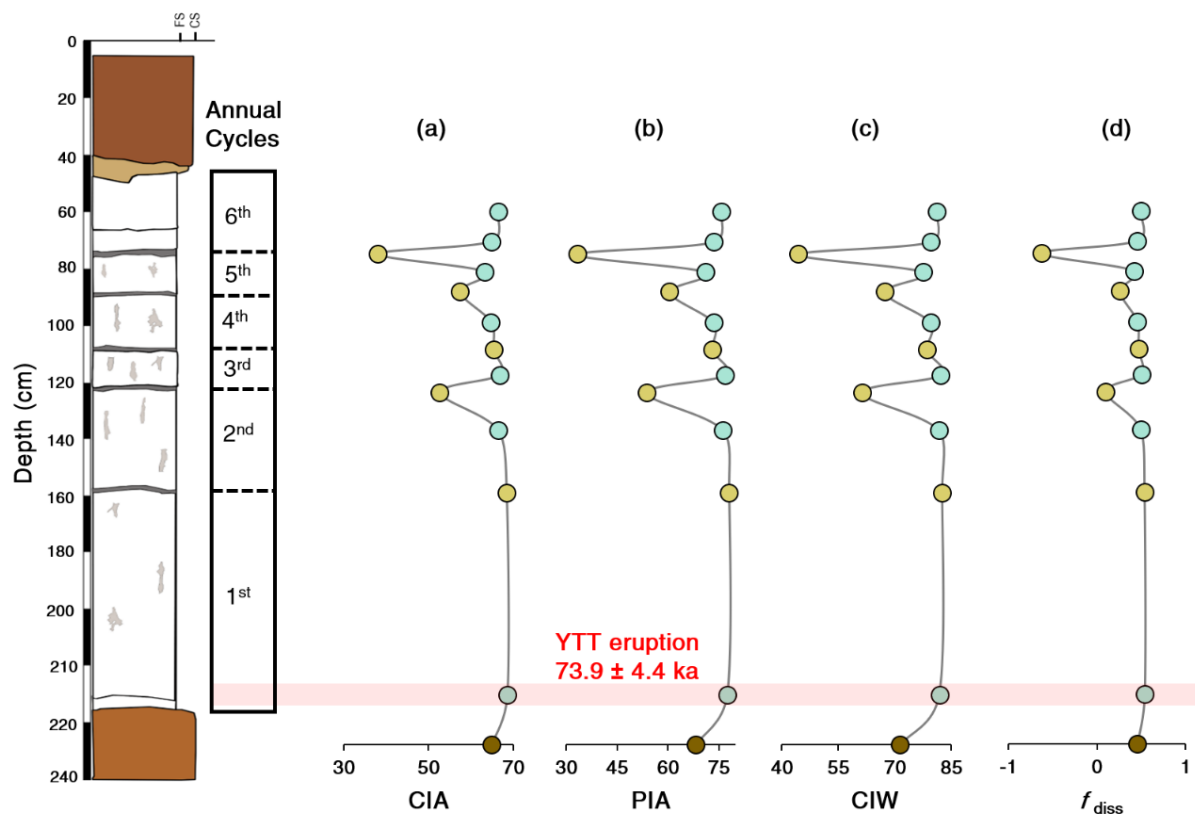


Fig. S24. Weathering indices – (a) Chemical index of alteration (CIA), (b) Plagioclase index of alteration, (c) Chemical index of weathering, and (d) Feldspar dissolution (f_{diss}). Legend: brown: pre-YTT layer, aqua blue: YTT/tephra layers and mustard: hardpan.

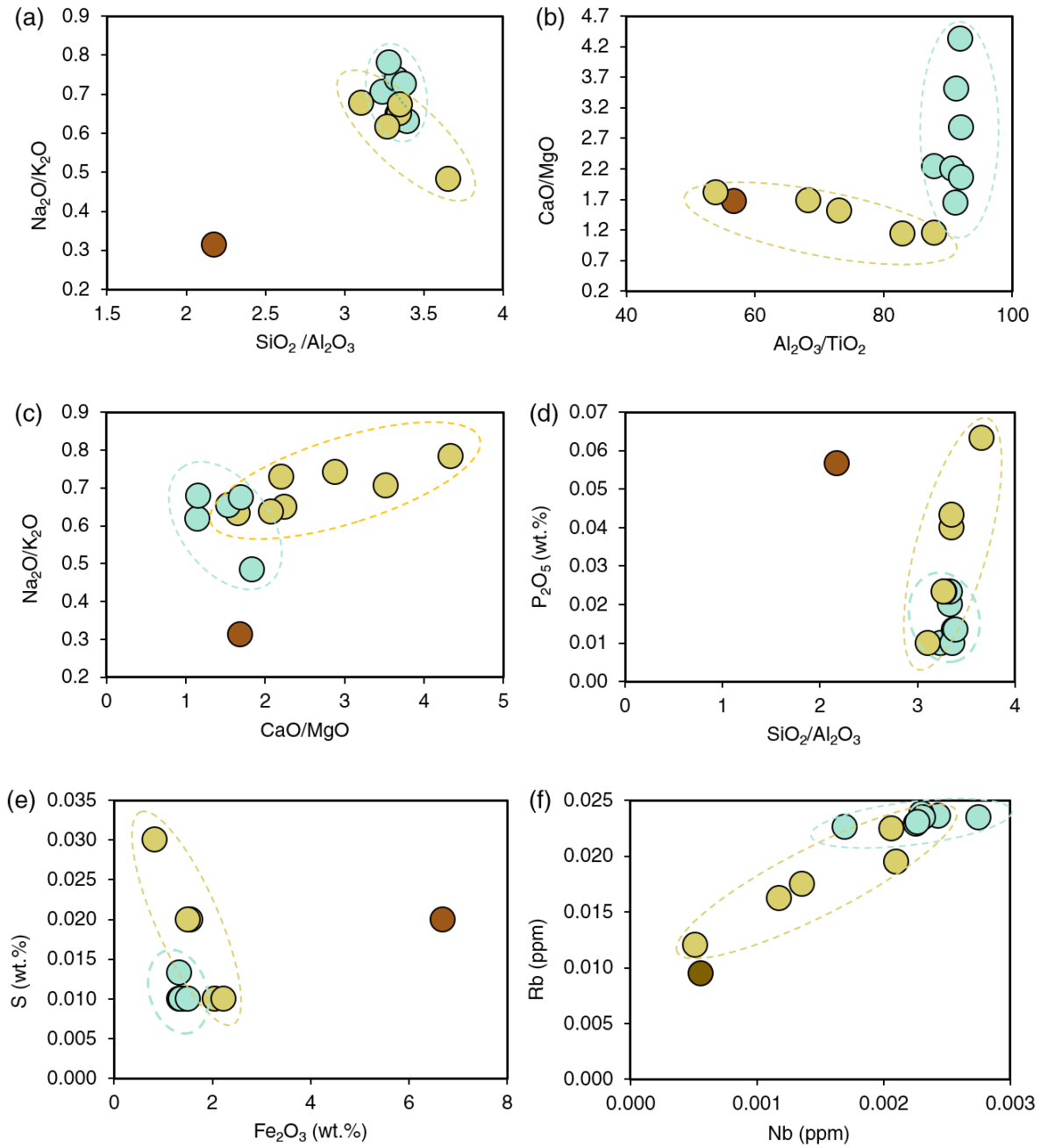


Fig. S25. Elemental proxies indicating YTT alteration based on post-depositional processes – (a-b) Comparison of base elements (Na_2O , K_2O , CaO , MgO) against ratio of immobile elements (Al_2O_3 , SiO_2 , TiO_2) show influence of leaching and diageneses on alteration of YTT; (c) Comparison between alkali base element (Na_2O and K_2O) and alkaline base elements (CaO and MgO) show higher mobility of CaO and MgO during hardpan samples indicating early stage of alteration; (d) We observe mobility in Phosphorus in hardpan samples, related to alteration of apatite mineral; (e) Mobility in Sulphur in hardpan formation is related to Pyrrhotite weathering where Sulphur tend to leach during alteration process; (f) Nb and Rb showing linear trend that indicates influence of hydration and leaching of YTT-derived silicate minerals. Legend: brown: pre-YTT layer, aqua blue: YTT/tephra layers and mustard: hardpan.

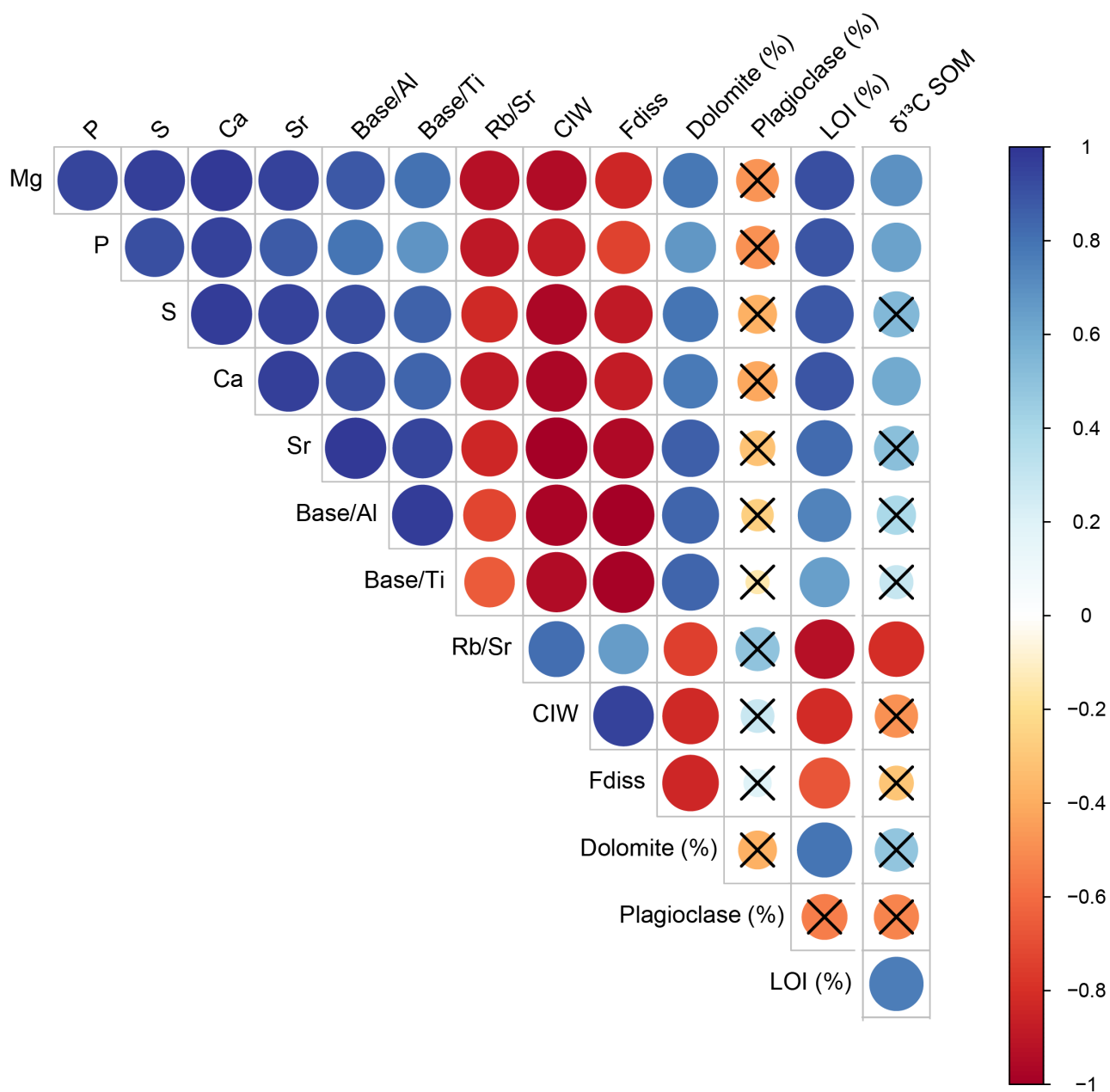


Fig. S26. Pearson correlation matrix of different palaeoenvironmental proxies used in the current study.

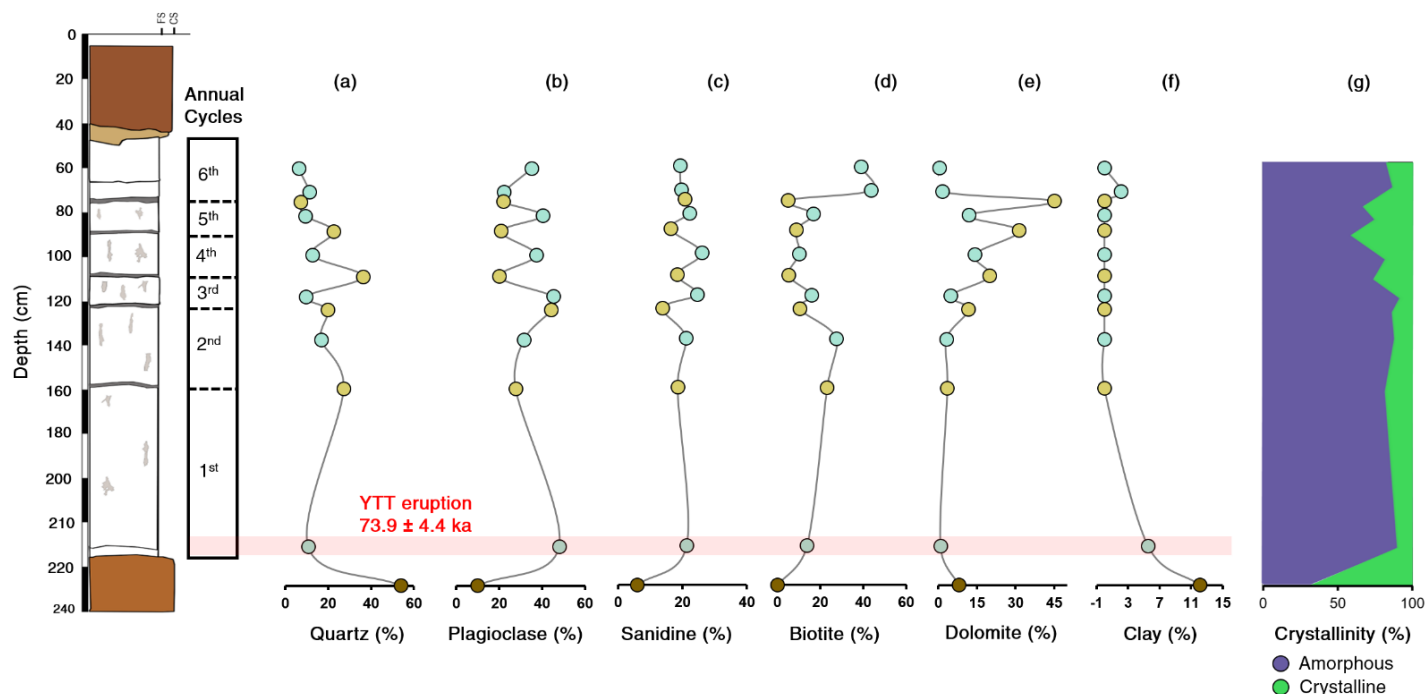


Fig. S27. Relative concentration (%) of major mineral groups based on XRPD dataset; (a) Quartz; (b) Plagioclase; (c) Sanidine; (d) Biotite; (e) Dolomite; (f) Clays; (g) Crystallinity (%). Mineralogical dataset indicates gradual increase in dolomite with subsequent hardpan, strongly related to loss of silicate minerals such as Plagioclase, Sanidine, and Biotite. Dotted line represents YTT event; Legend: brown: pre-YTT layer, aqua blue: YTT/tephra layers and mustard: hardpan.

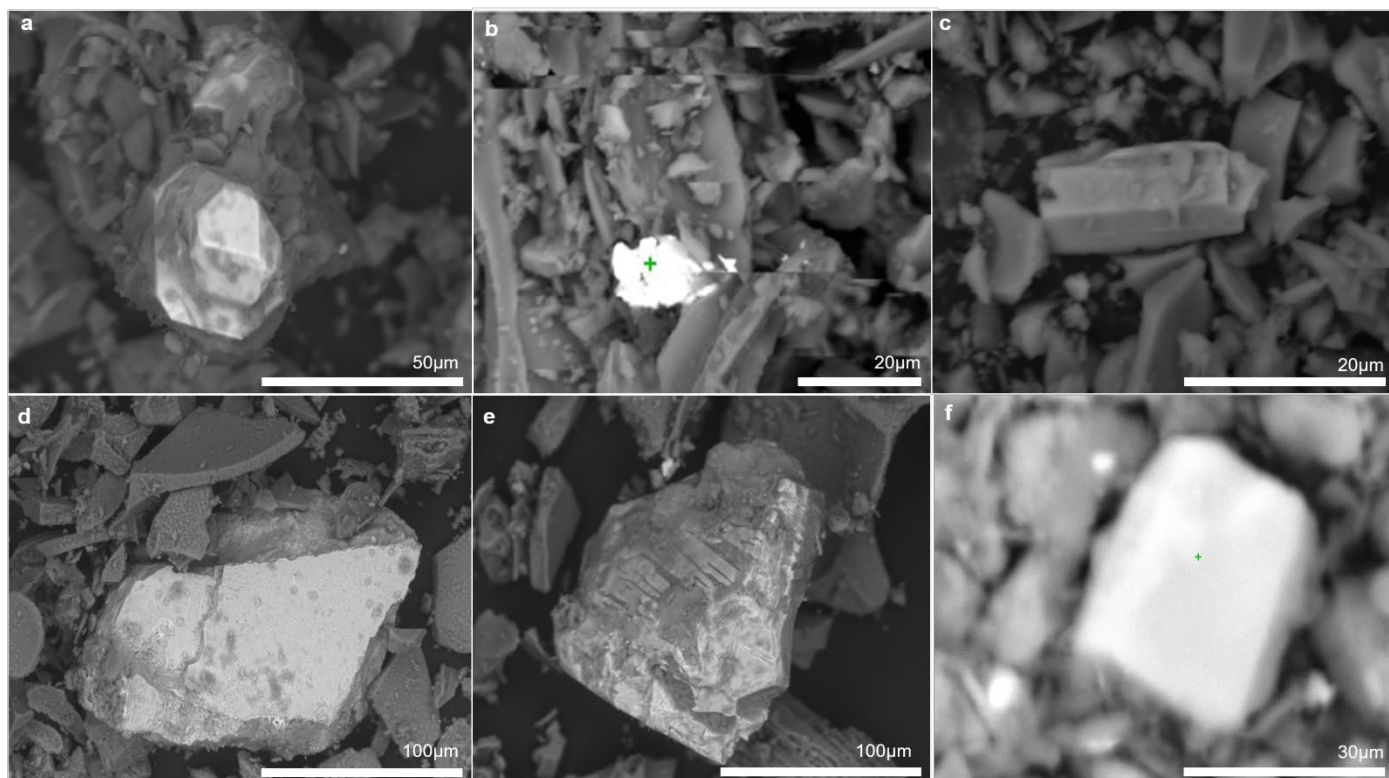


Fig. S28. SEM micrograph of different YTT minerals from Jwalapuram: (a) Zircon, (b) Chromite, (c) Amphibole, (d and e) Ilmenite and (f) Apatite

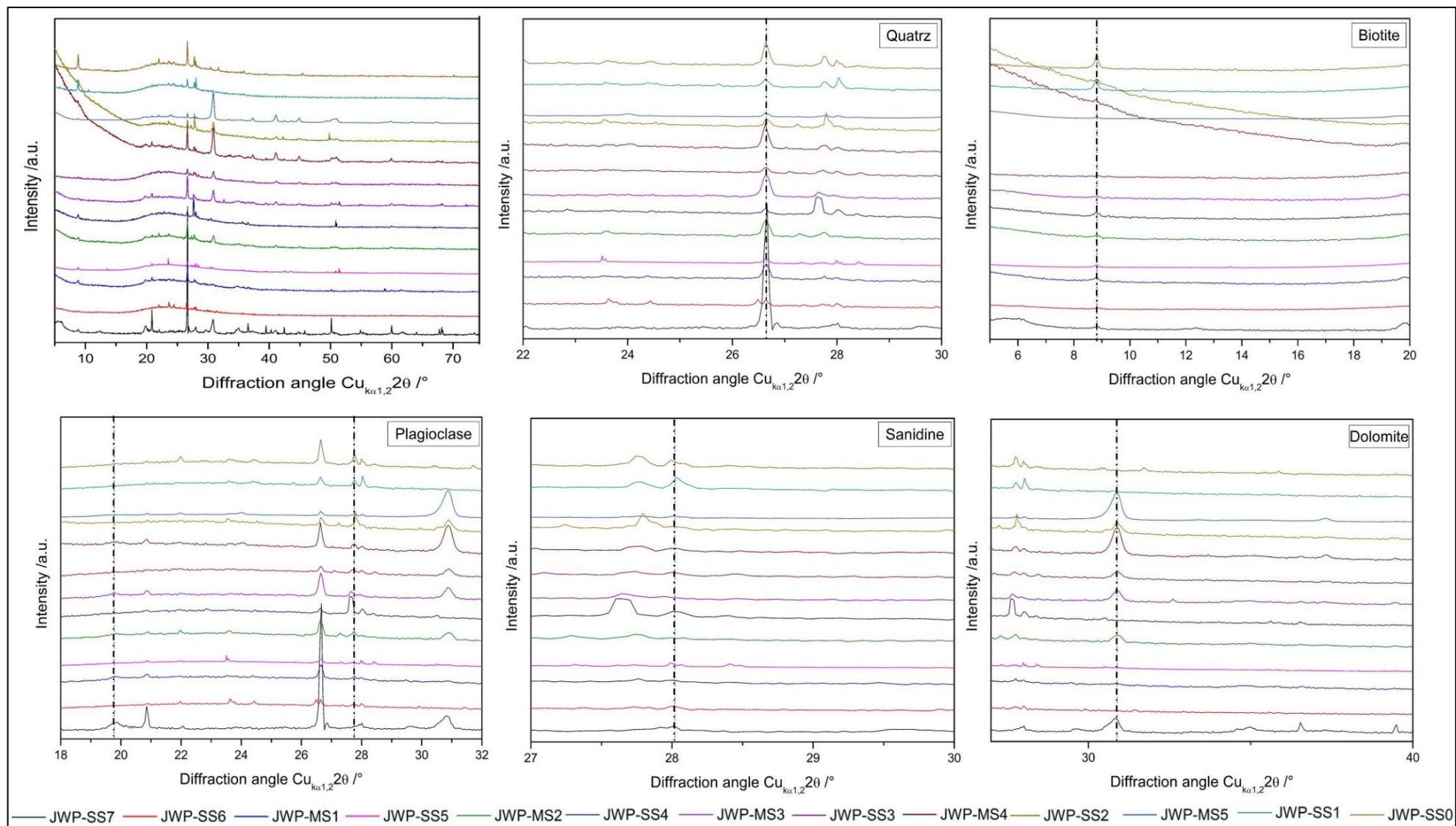


Fig. S29. Diffractogram of JWP2020 samples, showing major mineralogical group, including quartz, biotite, plagioclase, sanidine, and dolomite.

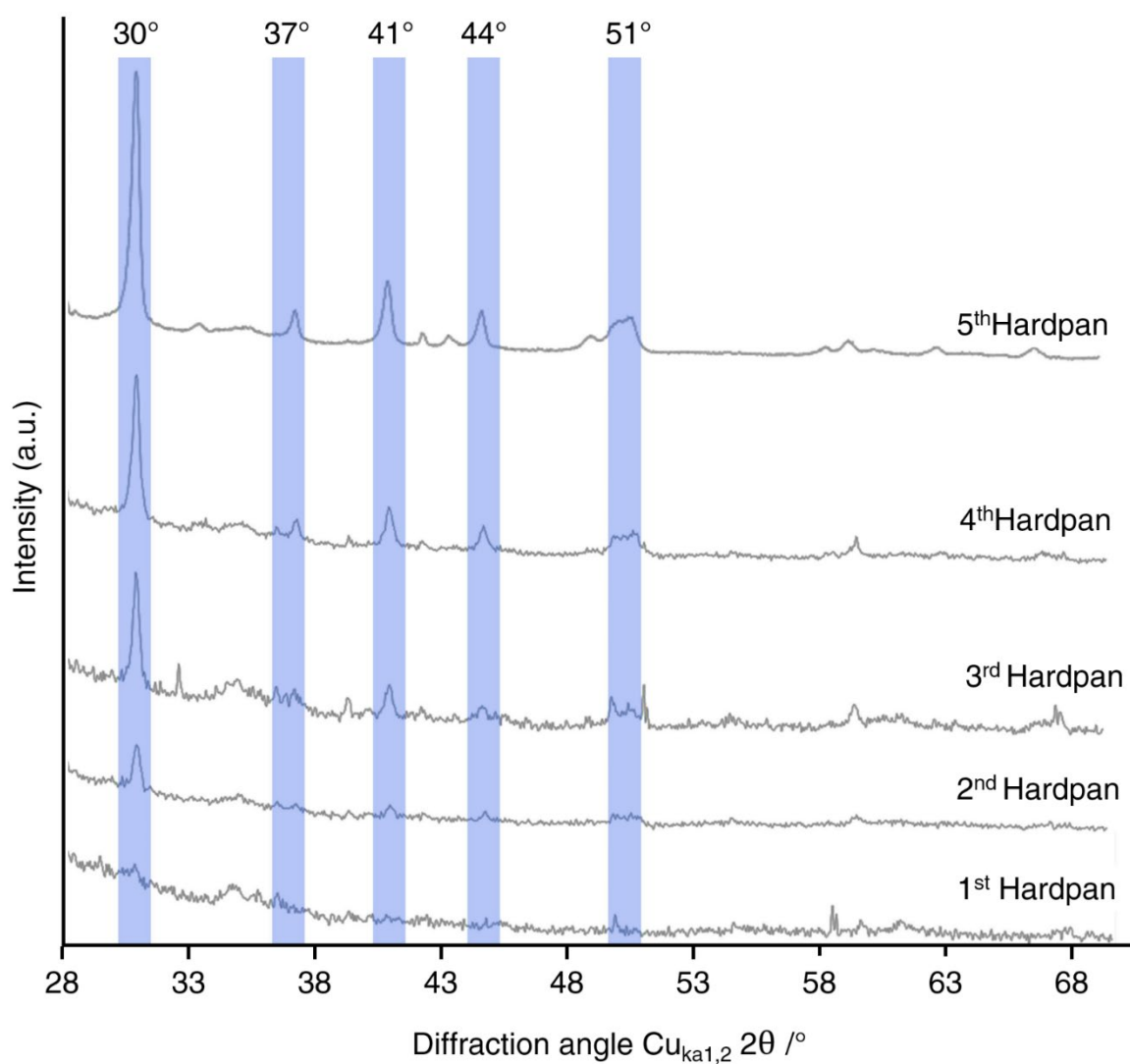


Fig. S30. Different reflection of dolomitic compound is observed in XRD diffractogram of Jwalapuram at 30.8°, 37°, 41°, 44° and 51°. Note the presence of dolomite in pre-YTT (SS7) sample. Increasing intensity of dolomite shows strong relation with increasing concentration of Ca and Mg in hardpan layers (MS1 – MS5). Gradual enrichment of dolomite corresponds with increasing concentration of Ca and Mg in hardpan layers.

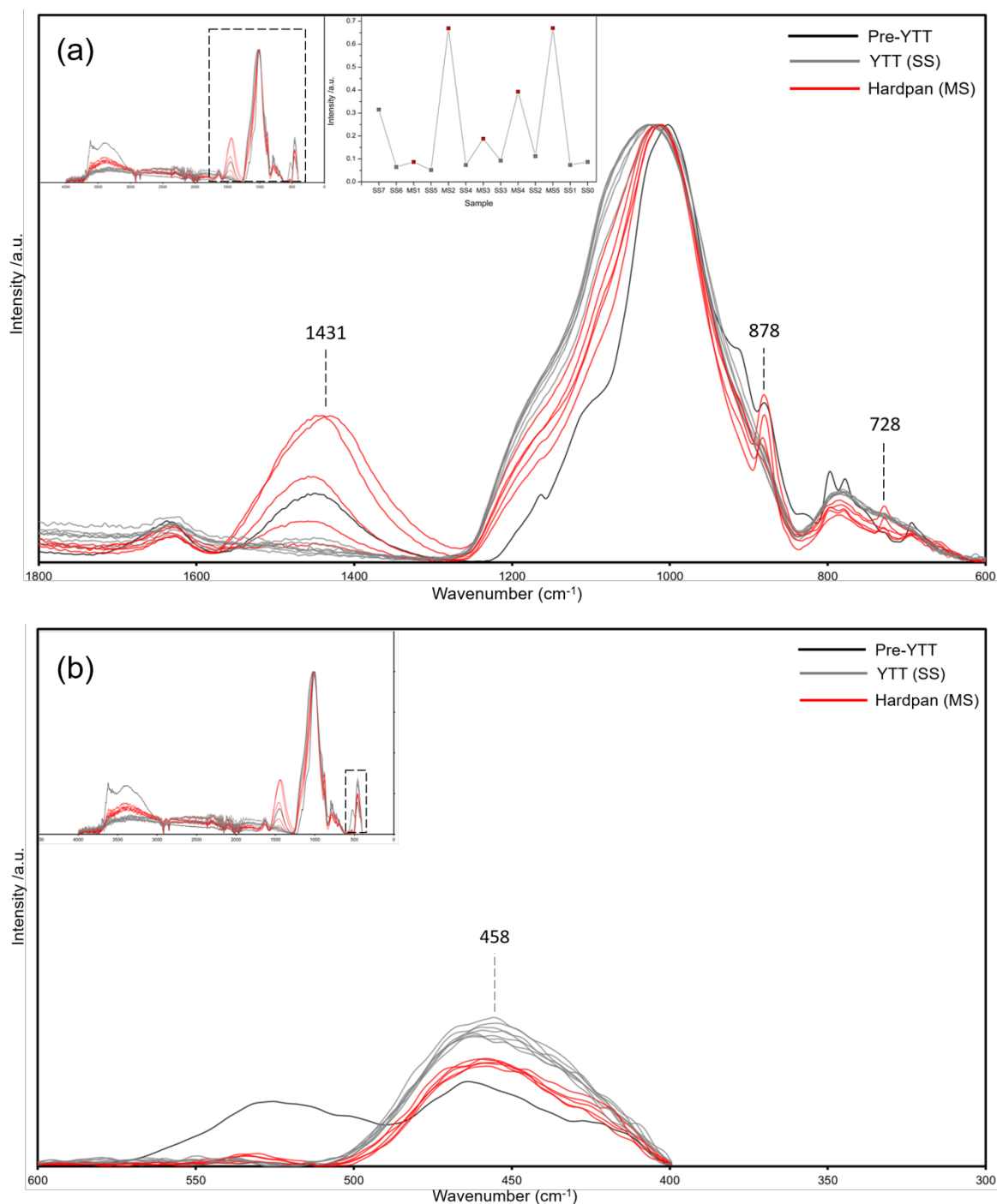


Fig. S31. ATR-FTIR spectra of Jwalapuram samples; (a) The ATR-FTIR spectra of Jwalapuram reflects significant intensities of bands originating from the vibrations of the group $(\text{CO}_3)^{2-}$ of dolomite (maxima at: 1431 cm^{-1} , 878 cm^{-1} , 728 cm^{-1}); (b) IR spectra also highlight probable variability in the relative intensity of SiO_2 in Tephra and hardpan samples.

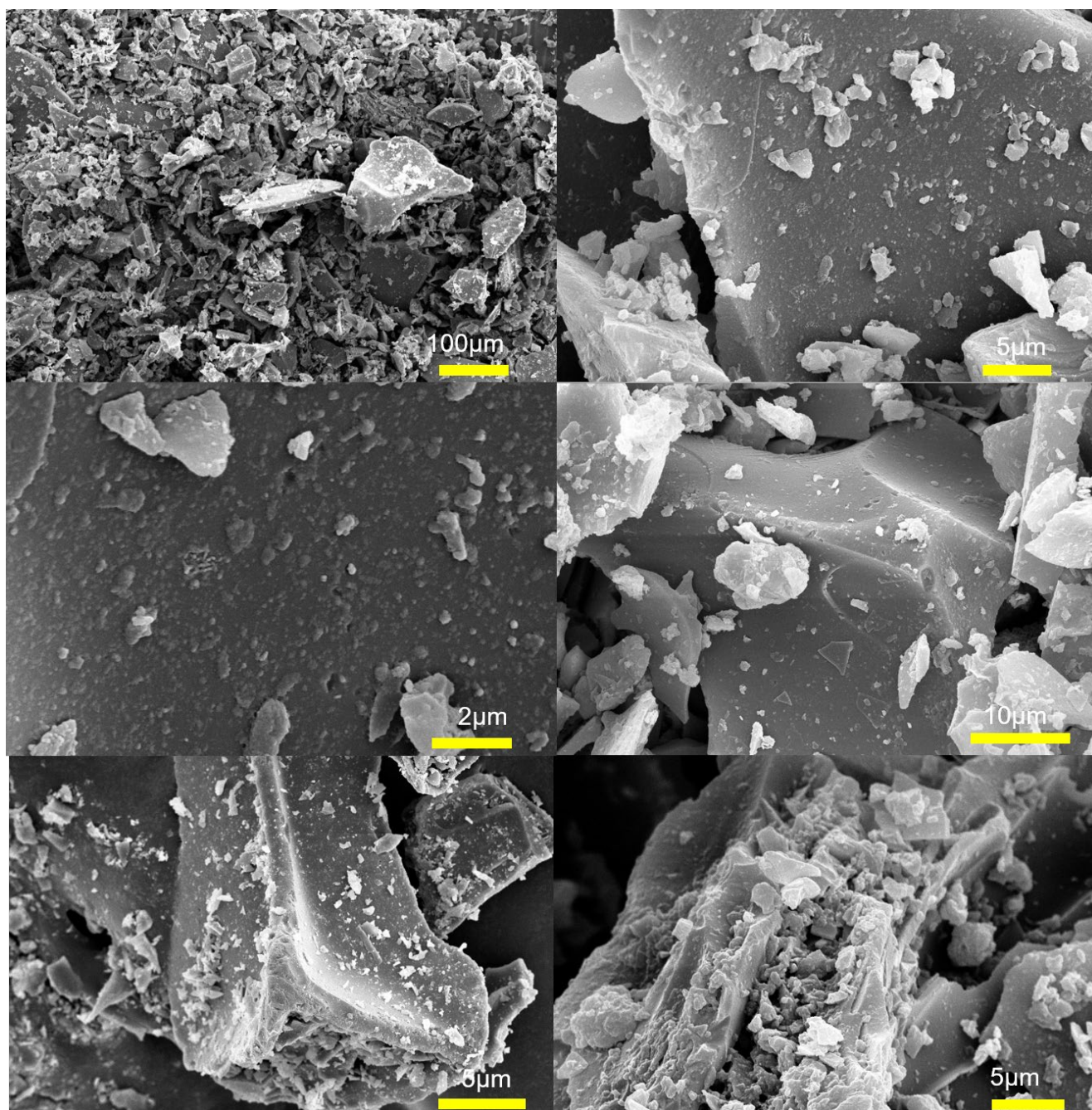


Fig. S32. SEM micrograph of YTT glass shards, taken in SE mode. Most of the glass shards have angular and sharp edges showing minimal physical alteration. Morphologically, the glass shards are broadly categorized into three different types as, (i) bubble wall shards with elongated and tri-radiate boundaries between vesicles, (ii) blocky glass masses with junctions of multiple vesicles, and (iii) light to medium brown-colored pumice grains showing tight packing of elongated vesicles.

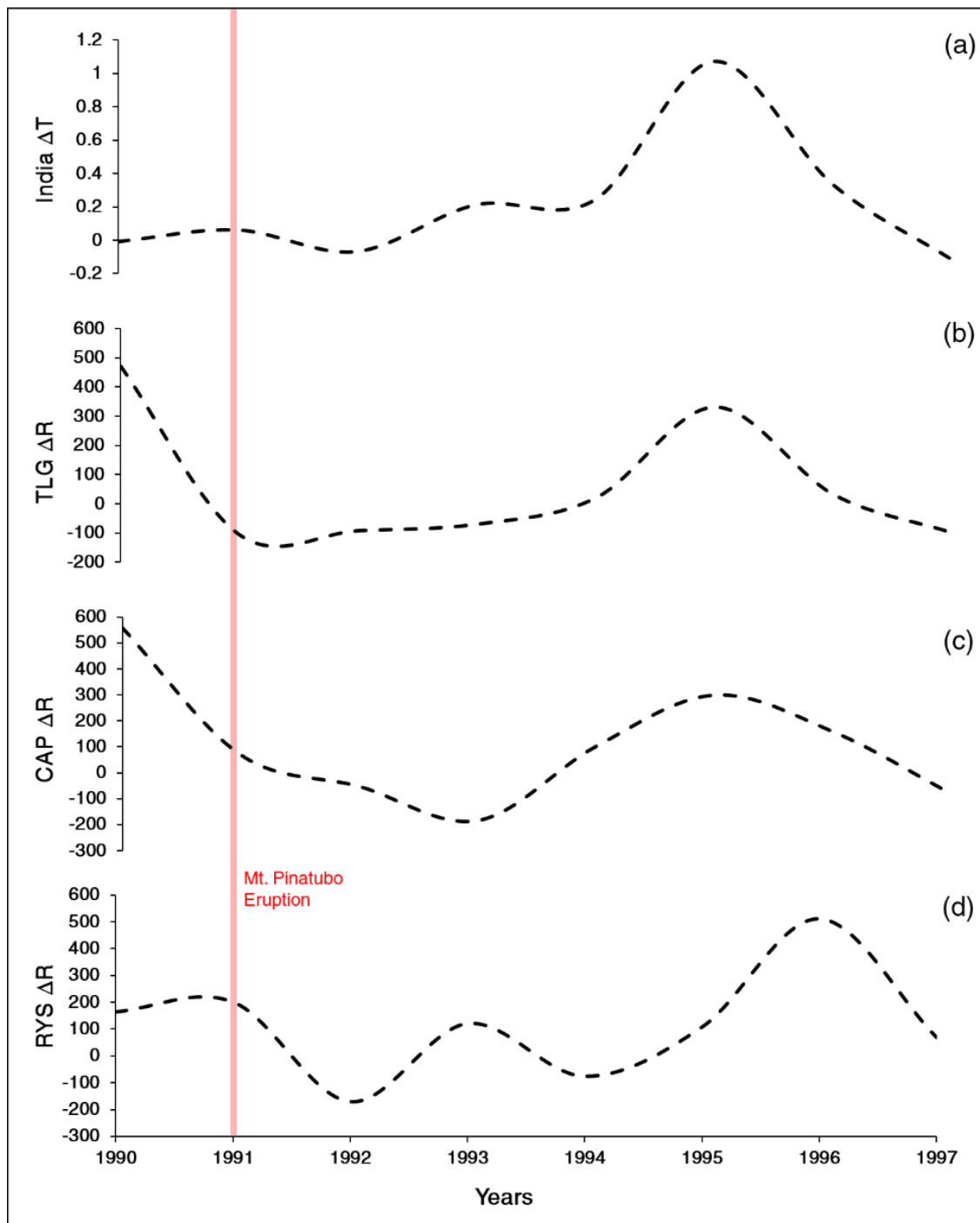


Fig. S33. Climate anomaly data from India spanning 1991 Mt. Pinatubo eruption; (a) Temperature anomaly (ΔT) data of India; (b – d) Rainfall anomaly (ΔR) data of Andhra Pradesh – Telangana (TLG), Coastal Andhra Pradesh (CAP), and Rayalseema (RYS). ΔT data show increasing warming between 1992-1995 indicating El Niño phase after Pinatubo eruption, ΔR data of different part of Andhra Pradesh show reduction in rainfall volume during 1991-1995. Note: Jwalapuram is situated in the Rayalseema province.

Table S1. Lithostratigraphy of YTT yielding sections of Jwalapuram; current work is based on geochemical analysis of YTT tephra (layer C) from JWP2020.

Strata	Description	Archaeology	Locality	Age (ka)
A	A deposit of yellow-brown silty sand containing gravel layer at base. Gravel is dispersed throughout the deposit, with varying concentrations in different sections, likely a result of cut and fill processes.	Middle Palaeolithic	JWP3, JWP23, JWP2020	35ka – 38ka
B	Yellow-brown pedogenically altered ash-rich silty sand. Higher concentration of volcanic ash at the basal part.	-	JWP3, JWP23, JWP2020	-
C	Light grey reworked volcanic ash (YTT) featuring a thin (~5 cm) basal layer of primary ash and six fining-upward beds separated by prominent, laterally extensive hardpans. The upper sections of each bed exhibit signs of microbial mat formation, ripple structures, and desiccation cracking. The base of this layer displays soft-sediment deformation structures.	-	JWP3, JWP23, JWP2020	~74ka
D	Reddish-brown pedogenically altered lacustrine/palludal clay deposit, with concentration of nodular calcrete at the base.	Middle Palaeolithic	JWP3, JWP22, JWP2020	71±8ka

Table S2. Molecular weathering and pedogenesis ratios used in the current study.

Elemental Ratio	Paedogenic Process	Associated factor	Reference
Si/Al	Hydrolysis	Clayeness, Fluvial Strength, and Precipitation	Price and Velbel(36); Macias and Arbestain(51)
Al/Ti	Acidification	Temperature, Forestation, and Soil pH	Ticha et al.(52)
Ca/Mg	Leaching and Precipitation	Evapotranspiration and Temperature	Fiantis et al.(53)
Ca/Na	Hydrolysis and Leaching	Weathering	Dahlgren et al.(54)
$\Sigma_{\text{Bases}}/\text{Al}$	Hydrolysis	Weathering	Sheldon and Tabor(37)
$\Sigma_{\text{Bases}}/\text{Ti}$	Leaching	Weathering	Rouzaut et al.(55)
Rb/Sr	Leaching	Precipitation and Soil Humidity	Ouyang et al.(13)

Table S3. Summary of weathering indices used in the current study. Note: >50 values in CIA, CIW and PIA represent early weathering products.

Indices	Formula	Optimum Fresh value	Trend	Reference
Chemical Index of Alteration (CIA)	$(100)[\text{Al}_2\text{O}_3/(\text{Al}_2\text{O}_3+\text{CaO}+\text{Na}_2\text{O}+\text{K}_2\text{O})]$	50 onwards	Positive	Nesbit and Young(56)
Chemical Index of Weathering (CIW)	$(100)[\text{Al}_2\text{O}_3/(\text{Al}_2\text{O}_3+\text{CaO}+\text{Na}_2\text{O})]$	50 onwards	Positive	Maynard(57)
Plagioclase Index of Alteration (PIA)	$(100)[\text{Al}_2\text{O}_3/(\text{Al}_2\text{O}_3+\text{CaO}+\text{Na}_2\text{O}-\text{K}_2\text{O})]$	50 onwards	Positive	Roy et al.(58)
Feldspar Dissolution (f_{diss})	$100/\text{CIA}+2$	—	Negative	Deng et al.(41)

Table S4. Detailed palaeoclimatic and palaeopedological synthesis tephra deposit at Jwalapuram (JWP3 and JWP2020) in chronological order (first annual monsoonal cycle to sixth monsoonal cycle). Note: Aqua colour represent tephra deposition episodes, indicating wetter conditions; Mustard colour represent hardpan layer representing dry seasons.

Unit	Layer	Characteristics
C1 (1st Annual Monsoonal cycle)	1st Tephra layer (SS6)	<ul style="list-style-type: none"> - The basal ~5 cm of unit C1 is a primary air-fall YTT deposit, dated back to 73.9 ± 4.4 ka. It rests on reddish-brown clayey silt (layer D). - Pre-YTT stratum D yielded several MP artefacts at the locality of JWP22, dated back to 71 ± 8 ka, just before the primary ashfall. This suggests that hominins may have occupied the site during the ~74 ka YTT event. - Earlier sedimentological and geoarchaeological work demonstrated that ~74 ka Jwalapuram was a palaeowetland or swamp-like environment. Hominins occupied the margins of these swamps during different time intervals. - Stratigraphic features like soft sediment deformation and bleeding of underlying sediment, ripple marks, and upward fining of tephra suggest that the air-fall tephra was deposited in an aqueous setting. - The particle size distribution (PSD) is more varied in the basal YTT, containing both finer and coarser particles compared to other tephra layers. Overall, the PSD is similar to other ash strata, with mode values ranging from 44 μm to 88 μm. - The magnetic susceptibility (MS) is slightly higher ($54.9 \times 10^{-8} \text{ m}^3/\text{kg}$) than that of the overlying tephra layer. This increase could be due to the presence of a minor amount of sediment from the underlying layer D deposit. - The primary YTT contains the highest Total Organic Matter (TOM = 3.7%) compared to above-lying tephra units and other litho-units (layer A, B, and D). - The basal YTT is predominantly composed of an amorphous fraction (91.6%), marking the first phase of YTT deposition in the Jurreru valley. It is also complemented by a sudden surge in the concentration of SiO_2 (72.1 wt.%), Al_2O_3 (12.9 wt.%), Na_2O (3.9 wt.%), and K_2O (3.3 wt.%). - The carbonate content is the lowest (1.6%) compared to subsequent tephra units. It coincides with lower concentrations of dolomite (0.8%) and mobile elements like CaO (0.89 wt.%) and MgO (0.29 wt.%). - Silicate weathering proxies ($\Sigma_{\text{Bases}}/\text{Al}_2\text{O}_3$: 0.46 and $\Sigma_{\text{Bases}}/\text{TiO}_2$: 42.76) indicate no signs of chemical weathering. - An increase in Rb/Sr (2.37) values suggest higher soil moisture and rainfall, coinciding with an increase in organic matter concentration and a negative excursion in the palaeovegetation proxy $\delta^{13}\text{C}_{\text{SOM}}$ (-26.33‰). - The primary ash-fall was followed by the rapid mobilization and redeposition of tephra from higher

		<p>altitudes to low-lying regions, primarily due to sheet wash by seasonal rain.</p> <ul style="list-style-type: none"> - The first YTT redeposition phase occurred immediately after the initial air-fall during the first annual monsoonal cycle, as no signs of sediment break or hardpan are observed between primary and redeposited tephra. - This unit shows upward fining features and ripple marks, suggesting the redeposition of YTT occurring in an aquatic setting. - PSD data show a gradual upward increase in the finer silty fraction of the C1 unit, explaining the upward fining feature of the tephra unit. - This is the thickest tephra unit compared to subsequent units, primarily due to large-scale removal of unconsolidated tephra and rapid redeposition into topographic low areas like JWP3 and JWP2020. - The rapid redeposition of tephra also led to the burial of local vegetation, resulting in a dense concentration of rhizoliths. Few upright tree fossils were also observed in-situ in the tephra deposit at different YTT localities. The ideal preservation of such features is primarily due to rapid burial by the thick tephra unit. - Elemental and mineralogical characteristics of the redeposited tephra are similar to the primary air-fall tephra, highlighting its relative purity and no mixing of autochthonous terrigenous material.
	<p>1st Hardpan layer (MS1)</p>	<ul style="list-style-type: none"> - The first reworked tephra unit is capped by a thick, cemented greyish-brown hardpan layer. - Following the deposition of tephra, plants begin to take root and grow on the surface. Animals such as insects, crustaceans, and worms create tracks and burrows both on the surface and within the ash, forming intricate burrowing systems and chambers. This colonization by living organisms might occur in a sub-aqueous environment or in a sub-aerial habitat after the lake or swamp has dried out. Such ichno fossils of biogenic processes are observed all over the hardpan. - PSD data indicate that hardpan is primarily formed of fine silty material, cemented by carbonate material. - The surface hardpan shows a drastic rise in magnetic susceptibility (from 40.2 to 101.4 x 10⁻⁸ m³/kg) and carbonate content by 6.6%. This cementation might have taken place due to the rapid drying of wet tephra, where dissolved minerals (like Ca and Mg) precipitated upwards and formed dolomitic duricrust. - There is a relative increase in the concentration of CaO (0.96 wt.%) and MgO (1.16 wt.%) compared to the underlying tephra layer. A similar increase is also observed in the concentration of dolomite (3.5%). This is inversely reflected in the concentration of immobile elements (SiO₂: 68.8 wt.%, Al₂O₃: 13.05 wt.%, Na₂O: 3.6 wt.%). - Precipitation proxies Rb/Sr (2.05) show a relative decrease in values, indicating drier conditions. This is further supported by an increase in δ¹³C_{SOM} (-22.18‰).

<p>C2 (2nd Annual Monsoonal cycle)</p>	<p>2nd Tephra layer (SS5)</p>	<ul style="list-style-type: none"> - The second tephra redeposition unit represents a wetter period, signifying the reactivation of the wetland or swamp. It is marked by a fall in MS (from 101.4 to $41.2 \times 10^{-8} \text{ m}^3/\text{kg}$) and carbonate content (from 6.6% to 1.2%). - There is an increase in the concentration of immobile elements (SiO_2: 71.4 wt.%, Al_2O_3: 12.4 wt.%, Na_2O: 3.64 wt.%, K_2O: 3.8 wt.%) and a decrease in the concentration of mobile elements (CaO: 1.01 wt.%, MgO: 0.85 wt.%, P_2O_5: 0.013 wt.%) and the trace element Sr (0.01 ppm). - The ash is likely redeposited through monsoonal slope-wash and subsequent aeolian activity, resting on the first hardpan layer. - Similar upward fining of tephra is observed in this unit, confirming that the ash was deposited in an aquatic setting. - Palaeoprecipitation proxies Rb/Sr (2.02) show relatively constant values compared to unit C1 (including tephra and hardpan), suggesting a wetter environment. - This is complemented by a notable fall in $\delta^{13}\text{C}_{\text{SOM}}$ values (from -22.18‰ to -26.92‰), suggesting a change in vegetation, indicating a more humid environment.
	<p>2nd Hardpan layer (MS2)</p>	<ul style="list-style-type: none"> - As conditions became drier, it led to the desiccation of the exposed tephra surface and the formation of the second hardpan. The formation of the hardpan is reflected by a rise in MS ($84.5 \times 10^{-8} \text{ m}^3/\text{kg}$) and an increasing concentration of mobile elements and trace elements: CaO (7.72 wt.%), MgO (6.36 wt.%), P_2O_5 (0.043 wt.%), Sr (0.051 ppm), Nb (0.001 ppm), etc. - A similar increase is observed in CaCO_3 (12.05%) and a slight decrease in TOM (3.12%) compared to the underlying tephra layer. - Along with the enrichment of bases, there is a decreasing concentration of immobile elements (Al_2O_3: 9.4 wt.%, SiO_2: 53.5 wt.%, TiO_2: 0.17 wt.%) and silicate minerals (Sanidine: 13.9% and Biotite: 10.4%), which is positively correlated with increasing feldspar dissolution (f_{diss}: 0.10) and chemical weathering of silicates. - $\Sigma_{\text{Bases}}/\text{Al}_2\text{O}_3$ (1.16) and $\Sigma_{\text{Bases}}/\text{TiO}_2$ (79.4) of the second hardpan show an increase in hydrolysis and leaching compared to underlying layers, reflecting a rise in the intensity of chemical weathering. - A gradual positive excursion in the concentration of dolomite (11.7%) highlights the increase in evaporative and warming conditions. - Like the first hardpan, the second hardpan shows a drastic drop in Rb/Sr (from 2.02 to 0.32) values relative to the underlying redeposited tephra layer, pointing towards drying conditions. - Furthermore, $\delta^{13}\text{C}_{\text{SOM}}$ values (-21.69‰) of the second hardpan show an increase of -5.23‰, suggesting a change in vegetation and dry environmental conditions. - The unit C3 contains the highest concentration of plant fossils (rhizoliths) across the whole YTT deposit. It is likely that most of the surface vegetation died due to increasing warming, resulting in a dense concentration of plant fossils.

C3 (3rd Annual Monsoonal cycle)	3rd Tephra layer (SS4)	<ul style="list-style-type: none"> - Similar to other redeposited tephra layers (C1 and C2), this layer shows all stratigraphic signs of tephra being deposited in an aqueous medium. - There is a decreasing density of plant fossils (rhizoliths) in this tephra layer compared to the underlying tephra units (C1 and C2). - Like other redeposited tephra, there is an increase in the amorphous coarse (sand) fraction as reworked tephra is deposited in the valley (low-lying regions). The tephra redeposition episode is marked by a fall in MS ($41.4 \times 10^{-8} \text{ m}^3/\text{kg}$). However, it is important to note that the chemical composition (elemental and mineralogical) of reworked tephra is very similar to all other tephra layers and does not show any mixing of non-tephra material. - There is an increase in TOM (3.5%) and a decrease in CaCO_3 (1.44%) concentration. - The redeposition of tephra is marked by an increasing concentration of immobile elements (Al_2O_3: 12.6 wt.%, SiO_2: 72.1 wt.%, TiO_2: 0.17%) and a decrease in mobile elements (CaO: 0.85 wt.%, MgO: 0.57 wt.%, P_2O_5: 0.01 wt.%, S: 0.01 wt.%, Sr: 0.01 ppm), similar to the underlying tephra units. Furthermore, an increase in Rb/Sr (2.25) suggests a wetter environment during tephra redeposition. A negative excursion in $\delta^{13}\text{C}_{\text{SOM}}$ (-26.7‰) also indicates humid conditions.
	3rd Hardpan layer (MS3)	<ul style="list-style-type: none"> - Like previous units, redeposited tephra goes through desiccation, leading to the formation of the 3rd hardpan layer. The formation of hardpan is marked by an increase in the concentration of base elements (CaO: 2.39 wt.% and MgO: 2.93 wt.%), other mobile elements (S: 0.01 wt.%, P_2O_5: 0.02 wt.%, Sr: 0.02 ppm, Nb: 0.002 ppm), CaCO_3 (22.15%) and dolomite (20%). - We also observe a slight increase in MS ($47.5 \times 10^{-8} \text{ m}^3/\text{kg}$) and a decrease in TOM (2.63%). This is strongly correlated to the falling Rb/Sr (0.9) values, suggesting drier conditions. Further, this is also complemented by elevated $\Sigma_{\text{Bases}}/\text{Al}_2\text{O}_3$ (0.62) and $\Sigma_{\text{Bases}}/\text{TiO}_2$ (51.2) values, indicating an increase in the chemical weathering of silicate minerals. - An increase in $\delta^{13}\text{C}_{\text{SOM}}$ (-21.21‰) values suggests a change in vegetation and dry environmental conditions.
C4 (4th Annual Monsoonal cycle)	4th Tephra layer (SS3)	<ul style="list-style-type: none"> - Similar to previous units of redeposited tephra, this layer is geochemically alike and does not show any non-tephra input. - There is a slight increase in the density of rhizoliths and burrow activities, which could be related to post-depositional desiccation. - Like previous tephra units, it shows a fall in MS ($42.1 \times 10^{-8} \text{ m}^3/\text{kg}$) and CaCO_3 (3.32%) concentration, also reflected by a decrease in the concentration of mobile elements (CaO: 1.13 wt.%, MgO: 0.71 wt.%, P_2O_5: 0.01 wt.%, S: 0.01 wt.%, Sr: 0.01 ppm, Nb: 0.002 ppm) and an increase in immobile

		<p>elements (Al_2O_3: 12.4 wt.%, SiO_2: 71.04 wt.%, TiO_2: 0.17%).</p> <ul style="list-style-type: none"> - Lower concentration of dolomite and an increase in Rb/Sr (1.94) values suggest a fall in evaporative conditions and an increase in soil moisture, indicating wetter conditions during tephra redeposition. This is further complemented by a fall in $\delta^{13}\text{C}_{\text{SOM}}$ (-24.5‰) values, suggesting the same.
	4th Hardpan layer (MS4)	<ul style="list-style-type: none"> - Redeposited tephra is capped by another dolomite-rich hardpan layer, showing an increase in the concentration of base elements (CaO: 5.84 wt.% and MgO: 5.30 wt.%), trace elements (Sr: 0.04 ppm and Nb: 0.001 ppm), and other mobile elements (P_2O_5: 0.04 wt.% and S: 0.02 wt.%). It is important to note that the concentration of the aforementioned elements is relatively higher than in the preceding hardpan (i.e., the 3rd hardpan). A similar pattern is also observed in MS ($83.9 \times 10^{-8} \text{ m}^3/\text{kg}$) and the concentration of CaCO_3 (27.9%), which is inversely reflected in TOM (2.25%) concentration. - Relatively higher concentration of dolomite (31.3%) and lower Rb/Sr (0.39) values compared to the previous hardpan layer suggest that the current drying season is more intense than previous ones. A similar rise is also observed in chemical weathering proxies ($\Sigma_{\text{Bases}}/\text{Al}_2\text{O}_3$: 0.62 and $\Sigma_{\text{Bases}}/\text{TiO}_2$: 54.85) and $\delta^{13}\text{C}_{\text{SOM}}$ (-22.7‰). - Large mudcracks observed in the upper part of the tephra layer likely formed due to rapid drying and desiccation of the tephra, as reflected by the aforementioned proxies.
C5 (5th Annual Monsoonal cycle)	5th Tephra layer (SS2)	<ul style="list-style-type: none"> - Stratigraphic features are similar to the underlying tephra units, suggesting that the tephra was deposited in an aquatic setting. - We observe a relative increase in the concentration of rhizoliths compared to the underlying tephra layers. - MS ($42.2 \times 10^{-8} \text{ m}^3/\text{kg}$), CaCO_3 (2.33%), and TOM (3.19%) values are relatively higher than those in other tephra units. - A similar trend is observed in the concentration of base elements (CaO: 2.18 wt.% and MgO: 1.35 wt.%) and other mobile elements (P_2O_5: 0.02 wt.%, S: 0.01 wt.%, Sr: 0.01 ppm). - Rb/Sr (1.29) values are comparatively lower than in the previous tephra layers, suggesting a weakening of precipitation and less humid conditions.
	5th Hardpan layer (MS5)	<ul style="list-style-type: none"> - Post-deposition, the exposed tephra layer underwent extreme desiccation, leading to the formation of the last hardpan layer in the YTT sequence of Jwalapuram. - Like unit C4, the tephra layer of C5 also exhibits numerous mudcracks, primarily formed due to desiccation and rapid drying of the tephra layer. - We observed a drastic increase in CaCO_3 (22.25%) concentration, followed by a relative decrease in TOM (2.84%) compared to the underlying tephra. - The concentration of base elements (CaO: 13.18 wt.% and MgO: 10.03 wt.%) and other mobile elements (P_2O_5: 0.06

		<p>wt.%, S: 0.03 wt.%, Sr: 0.09 ppm) is at its peak, which is inversely reflected in the immobile elements (Al_2O_3: 6.18 wt.%, SiO_2: 42.29 wt.%, TiO_2: 0.16 wt.%), showing the lowest concentration in the whole sequence.</p> <ul style="list-style-type: none"> - Chemical weathering proxies indicate the highest degree of chemical weathering of tephra-derived silicate minerals, complemented by relatively low concentrations of silicate minerals (plagioclase: 21.9%, sanidine: 20.8%, and biotite: 5%) compared to the underlying tephra unit. - The f_{diss} (-0.62) and chemical weathering proxies ($\Sigma_{\text{Bases}}/\text{Al}_2\text{O}_3$: 2.2, $\Sigma_{\text{Bases}}/\text{TiO}_2$: 118.9, CIA: 38.13, CIW: 33.37, and PIA: 44.51) suggest an intense level of silicate weathering, highlighted by the highest concentration of weathered products in the 5th hardpan layer. - A key highlight of this layer is the highest concentration of dolomite (45.2%), suggesting peak surface warming and highly evaporative conditions. - This is further complemented by the lowest Rb/Sr (0.13), indicating strong arid conditions. A similar increase is observed in $^{13}\text{C}_{\text{SOM}}$ (-22.82‰), showing a relative change in vegetation that is strongly correlated with the lower TOM (2.84‰) values. - The concentration trend of base elements, other mobile elements, palaeoprecipitation proxies, and dolomite shows a step-wise increase in chemical weathering of silicate minerals, likely related to gradually increasing surface warming, decreasing precipitation, and strong evaporative conditions. Although the 5th hardpan layer in the JWP2020 sequence marks the pinnacle of arid environmental conditions, it started building up from the 1st hardpan layer as reflected in most of the abovementioned proxies.
<p>C6 (6th Annual Monsoonal cycle)</p>	<p>6th Tephra layer (SS0 – SS1)</p>	<ul style="list-style-type: none"> - This is the last phase of tephra redeposition. Most of the residual mass of tephra from the surrounding region was mobilized and deposited in low-lying areas. The stratigraphic features are similar to previous tephra layers, suggesting that the tephra was deposited in aqueous conditions. - This layer has the lowest MS ($39.9 \times 10^{-8} \text{ m}^3/\text{kg}$) values compared to the entire YTT unit, followed by higher TOM (3.44‰) values. - We also observe the lowest density of rhizoliths compared to the previous layer. - Geochemical data highlight that the chemical composition of volcanic ash is similar to the primary YTT ash and does not show any mixing with terrigenous material. - Chemical weathering proxies ($\Sigma_{\text{Bases}}/\text{Al}_2\text{O}_3$: 0.51 and $\Sigma_{\text{Bases}}/\text{TiO}_2$: 47.13) show a decrease in values, suggesting minimal or no chemical weathering of silicate minerals. This is further supported by the lowest concentration of dolomite (0.3%) and a significant increase in the concentration of immobile elements (Al_2O_3: 13.01 wt.%, SiO_2: 71.52 wt.%, TiO_2: 0.18 wt.%).

		<ul style="list-style-type: none"> - Similar trends are observed in the concentration of base elements (CaO: 0.89 wt.% and MgO: 0.35 wt.%) and other mobile elements (P₂O₅: 0.01 wt.%, S: 0.01 wt.%, Sr: 0.01 ppm). - Most of the proxy values are similar to the first tephra unit, probably indicating the end of the warming period, which also explains the absence of a hardpan in this unit. - Palaeoprecipitation (Rb/Sr: 2.31) and palaeovegetation (¹³C_{SOM}: -26.68‰) proxies support this conclusion, indicating a strengthening of precipitation and a return to a relatively humid environment. Phytolith analyses support this conclusion, with the appearance of grass morphotypes indicating a return of vegetation to the local landscape. - Unit C6 is followed by the deposition of a tephra-mixed sand horizon, which is the first non-tephra litho-unit formed since the beginning of the YTT phase. PDA shows a drastic increase in the sandy fraction, suggesting strengthened fluvial conditions. It is argued based on sedimentological data that by the conclusion of the C6 phase, the lake or swamp had dried up, largely due to being clogged by substantial amounts of volcanic ash. The overall geomorphology and hydrology of the valley were significantly transformed by the ash deposits and subsequent ash redeposition events. It is likely that the pre-ash-fall lacustrine or palustrine environment in the valley did not re-establish itself in the post-Toba period.
--	--	--

References

1. M. Petraglia, *et al.*, Middle Paleolithic Assemblages from the Indian Subcontinent Before and After the Toba Super-Eruption. *Science* (1979) **317**, 114–116 (2007).
2. M. D. Petraglia, P. Ditchfield, S. Jones, R. Korisettar, J. N. Pal, The Toba volcanic super-eruption, environmental change, and hominin occupation history in India over the last 140,000 years. *Quaternary International* **258**, 119–134 (2012).
3. S. C. Jones, Palaeoenvironmental response to the ~74 ka Toba ash-fall in the Jurreru and Middle Son valleys in southern and north-central India. *Quat Res* **73**, 336–350 (2010).
4. M. Haslam, *et al.*, The 74 ka Toba super-eruption and southern Indian hominins: Archaeology, lithic technology and environments at Jwalapuram Locality 3. *J Archaeol Sci* **37**, 3370–3384 (2010).
5. M. Haslam, *et al.*, A southern Indian Middle Palaeolithic occupation surface sealed by the 74 ka Toba eruption: Further evidence from Jwalapuram Locality 22. *Quaternary International* **258**, 148–164 (2012).

6. C. Oppenheimer, *Eruptions that shook the world* (Cambridge University Press, 2011).
7. S. C. Jones, The Toba supervolcanic eruption: Tephra-fall deposits in India and paleoanthropological implications. *Vertebrate Paleobiology and Paleoanthropology* 173–200 (2007). https://doi.org/10.1007/1-4020-5562-5_8.
8. J. Blinkhorn, A. G. Parker, P. Ditchfield, M. Haslam, M. Petraglia, Uncovering a landscape buried by the super-eruption of Toba, 74,000 years ago: A multi-proxy environmental reconstruction of landscape heterogeneity in the Jurreru Valley, south India. *Quaternary International* **258**, 135–147 (2012).
9. M. A. Kohler, T. J. Nordenson, W. E. Fox, *Evaporation from pans and lakes* (US Government Printing Office, 1955).
10. H. Achyuthan, N. Shankar, M. Braida, S. M. Ahmad, Geochemistry of calcretes (calic palaeosols and hardpan), Coimbatore, Southern India: Formation and Paleoenvironment. *Quaternary International* **265**, 155–169 (2012).
11. O. Kwiecien, *et al.*, What we talk about when we talk about seasonality – A transdisciplinary review. *Earth Sci Rev* [Preprint] (2022).
12. D. Fiantis, M. Nelson, J. Shamshuddin, T. B. Goh, E. Van Ranst, Determination of the Geochemical Weathering Indices and Trace Elements Content of New Volcanic Ash Deposits from Mt. Talang (West Sumatra) Indonesia. *Eurasian Soil Science* **43**, 1477–1485 (2010).
13. C. Ouyang, *et al.*, The Rb/Sr Ratio Response to Paleo Precipitation Recorded by Lake Sediment from a Semi Closed Lake in Southwest China since 16.0 cal. ka BP. *Ekoloji Dergisi* (2019).
14. J. Warren, “Dolomite: occurrence, evolution and economically important associations” (2000).
15. S. E. Kaczmarek, J. M. Gregg, D. L. Bish, H. G. Machel, B. W. Fouke, Dolomite, very high-magnesium calcite, and microbes— implications for the microbial model of dolomitization. *SEPM Special Publications* **109**, 7–20 (2017).
16. N. Losano, *et al.*, Hydrologic remobilisation of tephra-fall deposits: A sedimentological analysis throughout fluvio-lacustrine systems of North-West Patagonia. *The Depositional Record* (2024).
17. A. J. Dugmore, *et al.*, The interpretative value of transformed tephra sequences. *J Quat Sci* **35**, 23–38 (2020).
18. A. Folch, A review of tephra transport and dispersal models: Evolution, current status, and future perspectives. *Journal of Volcanology and Geothermal Research* **235**, 96–115 (2012).
19. S. Pouget, M. Bursik, G. Rogova, Tephra redeposition and mixing in a late-glacial hillside basin determined by fusion of clustering analyses of glass-shard geochemistry. *J Quat Sci* **29**, 789–802 (2014).
20. M. D. Shapley, B. P. Finney, Lake morphometry controls the remobilization and long-term geochemical imprint of distal tephra deposition. *J Paleolimnol* **53**, 309–320 (2015).

21. D. Beigt, G. Villarosa, V. Outes, E. A. Gómez, G. Toyos, Remobilized Cordón Caulle 2011 tephra deposits in north-Patagonian watersheds: Resedimentation at deltaic environments and its implications. *Geomorphology* **341**, 140–152 (2019).
22. X. Bolós, J. L. Macías, Y. Z. E. Ocampo-Díaz, C. Tinoco, Implications of reworking processes on tephra distribution during volcanic eruptions: The case of Parícutin (1943–1952, western Mexico). *Earth Surf Process Landf* **46**, 3143–3157 (2021).
23. N. A. Cutler, O. M. Shears, R. T. Streeter, A. J. Dugmore, Impact of small-scale vegetation structure on tephra layer preservation. *Sci Rep* **6** (2016).
24. J. R. M. Allen, B. Huntley, Effects of tephra falls on vegetation: A Late-Quaternary record from southern Italy. *Journal of Ecology* **106**, 2456–2472 (2018).
25. K. Wutke, *et al.*, Geochemical properties and environmental impacts of seven Campanian tephra layers deposited between 40 and 38 ka BP in the varved lake sediments of Lago Grande di Monticchio, southern Italy. *Quat Sci Rev* **118**, 67–83 (2015).
26. C. S. Lane, *et al.*, The Late Quaternary tephrostratigraphy of annually laminated sediments from Meerfelder Maar, Germany. *Quat Sci Rev* **122**, 192–206 (2015).
27. A. J. Dugmore, *et al.*, The interpretative value of transformed tephra sequences. *J Quat Sci* **35**, 23–38 (2020).
28. M. P. Kirkbride, A. J. Dugmore, Glaciological response to distal tephra fallout from the 1947 eruption of Hekla, south Iceland. *Journal of Glaciology* **49**, 420–428 (2003).
29. V. Ponomareva, M. Portnyagin, S. M. Davies, Tephra without borders: Far-reaching clues into past explosive eruptions. *Frontiers in Earth Sciences* [Preprint] (2015).
30. B. D. Collins, T. Dunne, Thirty years of tephra erosion following the 1980 eruption of Mount St. Helens. *Earth Surf Process Landf* **44**, 2780–2793 (2019).
31. E. Gatti, *et al.*, Depositional processes of reworked tephra from the Late Pleistocene Youngest Toba Tuff deposits in the Lenggong Valley, Malaysia. *Quaternary Research (United States)* **79**, 228–241 (2013).
32. D. G. Froese, G. D. Zazula, A. V. Reyes, Seasonality of the late Pleistocene Dawson tephra and exceptional preservation of a buried riparian surface in central Yukon Territory, Canada. *Quat Sci Rev* **25**, 1542–1551 (2006).
33. S. Wulf, M. Kraml, A. Brauer, J. Keller, J. F. W. Negendank, Tephrochronology of the 100ka lacustrine sediment record of Lago Grande di Monticchio (southern Italy). *Quaternary International* **122**, 7–30 (2004).
34. C. Martin-Puertas, *et al.*, Annual proxy data from lago grande di monticchio (southern Italy) between 76 and 112 ka: New chronological constraints and insights on abrupt climatic oscillations. *Climate of the Past* **10**, 2099–2114 (2014).
35. Y. H. Li, A Compendium of Geochemistry: Princeton, New Jersey. [Preprint] (2000).
36. J. R. Price, M. A. Velbel, Chemical weathering indices applied to weathering profiles developed on heterogeneous felsic metamorphic parent rocks. *Chem Geol* **202**, 397–416 (2003).

37. N. D. Sheldon, N. J. Tabor, Quantitative paleoenvironmental and paleoclimatic reconstruction using paleosols. *Earth Sci Rev* **95**, 1–52 (2009).
38. L. R. Kump, S. L. Brantley, M. A. Arthur, Chemical weathering, atmospheric CO₂, and climate. *Annu Rev Earth Planet Sci* **28**, 611–667 (2000).
39. J. Z. Williams, J. Z. Bandstra, D. Pollard, S. L. Brantley, The temperature dependence of feldspar dissolution determined using a coupled weathering-climate model for Holocene-aged loess soils. *Geoderma* **156**, 11–19 (2010).
40. X. Li, *et al.*, Globally elevated chemical weathering rates beneath glaciers. *Nat Commun* **13** (2022).
41. K. Deng, S. Yang, Y. Guo, A global temperature control of silicate weathering intensity. *Nat Commun* **13** (2022).
42. H. W. Nesbitt, R. E. Wilson, Recent chemical weathering of basalts. *Am J Sci* **292**, 740–777 (1992).
43. B. P. Ruxton, Measures of the degree of chemical weathering of rocks. *J Geol* **76**, 518–527 (1968).
44. L. Harnois, The CIW index: A new chemical index of weathering. *Sediment Geol* **55**, 319–322 (1988).
45. V. B. Asio, R. Jahn, Weathering of Basaltic Rock and Clay Mineral Formation in Leyte, Philippines. (2007).
46. T. Bonatitzky, F. Ottner, E. Erlendsson, G. Gísladóttir, Weathering of tephra and the formation of pedogenic minerals in young Andosols, South East Iceland. *Catena (Amst)* **198** (2021).
47. B. V. Óskarsson, M. S. Riishuus, Ó. Arnalds, Climate-dependent chemical weathering of volcanic soils in Iceland. *Geoderma* **189**, 635–651 (2012).
48. H. W. Nesbitt, G. M. Young, Formation and diagenesis of weathering profiles. *J Geol* **97**, 129–147 (1989).
49. P. V. Brady, The effect of silicate weathering on global temperature and atmospheric CO₂. *J Geophys Res* **96** (1991).
50. S. W. Bailey, Tracking the fate of plagioclase weathering products: Pedogenic and human influences. *Biogeochemical Cycles: Ecological Drivers and Environmental Impact* 151–162 (2020). <https://doi.org/10.1002/9781119413332.CH7>.
51. F. Macías, M. Camps-Arbestain, A biogeochemical view of the world reference base soil classification system: Homage to Ward Chesworth. *Advances in Agronomy* **160**, 295–342 (2020).
52. A. Tichá, D. Vondrák, A. Moravcová, R. Chiverrell, P. Kuneš, Climate-related soil saturation and peatland development may have conditioned surface water brownification at a central European lake for millennia. *Science of The Total Environment* **858**, 159982 (2023).

53. D. Fiantis, M. Nelson, J. Shamshuddin, T. B. Goh, E. Van Ranst, Leaching experiments in recent tephra deposits from Talang volcano (West Sumatra), Indonesia. *Geoderma* **156**, 161–172 (2010).
54. R. A. Dahlgren, F. C. Ugolini, W. H. Casey, Field weathering rates of Mt. St. Helens tephra. *Geochim Cosmochim Acta* **63**, 587–598 (1999).
55. S. Rouzaut, V. A. Campodonico, A. I. Pasquini, Weathering and paleoprecipitation indices in a Late Pleistocene–Holocene loess–paleosol sequence in central Argentina. *Environ Earth Sci* **80** (2021).
56. Hw. Nesbitt, G. M. Young, Early Proterozoic climates and plate motions inferred from major element chemistry of lutites. *Nature* **299**, 715–717 (1982).
57. J. B. Maynard, Chemistry of modern soils as a guide to interpreting Precambrian paleosols. *Journal of Geology* **100**, 279–289 (1992).
58. P. D. Roy, *et al.*, Geochemistry of late Quaternary tephra-sediment sequence from north-eastern Basin of Mexico (Mexico): implications to tephrochronology, chemical weathering and provenance. *Revista mexicana de ciencias geológicas* **29**, 24–38 (2012).
59. J. Longman, *et al.*, Release of tephra-hosted iron during early diagenesis fingerprinted by iron isotopes. *Earth Planet Sci Lett* **605**, 118016 (2023).
60. F. De Vleeschouwer, B. Van Vliët Lanoé, N. Fagel, Long term mobilisation of chemical elements in tephra-rich peat (NE Iceland). *Applied Geochemistry* **23**, 3819–3839 (2008).
61. N. J. G. Pearce, B. V Alloway, C. Wickham, Correlating weathered, microphenocryst-rich, intermediate tephra: An approach combining bulk and single shard analyses from the Lepué Tephra, Chile and Argentina. *Quaternary International* **500**, 71–82 (2019).
62. M. Anda, S. Purwanto, A. Dariah, T. Watanabe, R. A. Dahlgren, A 200-year snapshot of soil development in pyroclastic deposits derived from the 1815 super explosive eruption of Mount Tambora in Indonesia. *Geoderma* **433** (2023).
63. T. Bonatotsky, F. Ottner, E. Erlendsson, G. Gísladóttir, Weathering of tephra and the formation of pedogenic minerals in young Andosols, South East Iceland. *Catena (Amst)* **198**, 105030 (2021).
64. J. L. Ratcliffe, *et al.*, Rapid carbon accumulation in a peatland following Late Holocene tephra deposition, New Zealand. *Quat Sci Rev* **246** (2020).
65. S. T. Goldsmith, A. E. Carey, W. B. Lyons, D. M. Hicks, Geochemical fluxes and weathering of volcanic terrains on high standing islands: Taranaki and Manawatu-Wanganui regions of New Zealand. *Geochim Cosmochim Acta* **72**, 2248–2267 (2008).
66. M. Alkhatib, A. Eisenhauer, Calcium and strontium isotope fractionation in aqueous solutions as a function of temperature and reaction rate; I. Calcite. *Geochim Cosmochim Acta* **209**, 296–319 (2017).
67. L. Yang, *et al.*, Coupled effects of temperature and solution compositions on metasomatic dolomitization: Significance and implication for the formation mechanism of carbonate reservoir. *J Hydrol (Amst)* **604**, 127199 (2022).

68. R. S. Arvidson, F. T. Mackenzie, The dolomite problem; control of precipitation kinetics by temperature and saturation state. *Am J Sci* **299**, 257–288 (1999).
69. S. E. Kaczmarek, B. P. Thornton, The effect of temperature on stoichiometry, cation ordering, and reaction rate in high-temperature dolomitization experiments. *Chem Geol* **468**, 32–41 (2017).
70. F. N. Sadooni, F. Howari, A. El-Saiy, Microbial dolomites from carbonate-evaporite sediments of the coastal sabkha of Abu Dhabi and their exploration implications. *Journal of Petroleum Geology* **33**, 289–298 (2010).
71. B. Shuman, Controls on loss-on-ignition variation in cores from two shallow lakes in the northeastern United States. *J Paleolimnol* **30**, 371–385 (2003).
72. O. Heiri, A. F. Lotter, G. Lemcke, Loss on ignition as a method for estimating organic and carbonate content in sediments: reproducibility and comparability of results. *J Paleolimnol* **25**, 101–110 (2001).
73. M. H. O’Leary, Carbon isotopes in photosynthesis. *Bioscience* **38**, 328–336 (1988).
74. J. G. Wynn, Paleosols, stable carbon isotopes, and paleoenvironmental interpretation of Kanapoi, Northern Kenya. *J Hum Evol* **39**, 411–432 (2000).
75. G. D. Farquhar, J. R. Ehleringer, K. T. Hubick, Carbon isotope discrimination and photosynthesis. *Annu Rev Plant Biol* **40**, 503–537 (1989).
76. G. Wang, *et al.*, Paleovegetation reconstruction using $\delta^{13}\text{C}$ of soil organic matter. *Biogeosciences* **5**, 1325–1337 (2008).
77. Z. Rao, *et al.*, Relationship between the stable carbon isotopic composition of modern plants and surface soils and climate: A global review. *Earth Sci Rev* **165**, 110–119 (2017).
78. A. F. Diefendorf, K. E. Mueller, S. L. Wing, P. L. Koch, K. H. Freeman, Global patterns in leaf ^{13}C discrimination and implications for studies of past and future climate. *Proceedings of the National Academy of Sciences* **107**, 5738–5743 (2010).
79. V. J. Hare, E. Loftus, A. Jeffrey, C. B. Ramsey, Atmospheric CO_2 effect on stable carbon isotope composition of terrestrial fossil archives. *Nat Commun* **9** (2018).
80. P. Meyers, S. H.- Palaeogeography, undefined Palaeoclimatology, undefined Palaeoecology, undefined 1993, An organic carbon isotopic record of glacial-postglacial change in atmospheric pCO_2 in the sediments of Lake Biwa, Japan. *Elsevier* **105**, 178 (1993).
81. J. G. Wynn, Carbon isotope fractionation during decomposition of organic matter in soils and paleosols: Implications for paleoecological interpretations of paleosols. *Palaeogeogr Palaeoclimatol Palaeoecol* **251**, 437–448 (2007).
82. B. Roy, S. Ghosh, P. Sanyal, Impact of monsoon, vegetation, and landscape on pedogenesis: A case study using organic and inorganic tracers from the Himalayan foreland sediments. *Palaeogeogr Palaeoclimatol Palaeoecol* **556**, 109854 (2020).
83. D. Xia, *Magnetic Studies of Tephra in Late Holocene Peats and Loessic Soils from SE Iceland* (The University of Liverpool (United Kingdom), 2003).

84. B. O. Guerrero, R. Thompson, J. U. Fucugauchi, Magnetic properties of lake sediments from Lake Chalco, central Mexico, and their palaeoenvironmental implications. *Journal of Quaternary Science: Published for the Quaternary Research Association* **15**, 127–140 (2000).
85. D. Fiantis, M. Nelson, E. Van Ranst, J. Shamshuddin, N. P. Qafoku, Chemical weathering of new pyroclastic deposits from Mt. Merapi (Java), Indonesia. *J Mt Sci* **6**, 240–254 (2009).
86. J. G. Wynn, M. I. Bird, V. N. L. Wong, Rayleigh distillation and the depth profile of $^{13}\text{C}/^{12}\text{C}$ ratios of soil organic carbon from soils of disparate texture in Iron Range National Park, Far North Queensland, Australia. *Geochim Cosmochim Acta* **69**, 1961–1973 (2005).
87. M. Singh, *et al.*, “Fingerprint of volcanic forcing on the ENSO-Indian monsoon coupling” (2020).
88. X. Fang, X. Zheng, X. Zhang, Correspondence between the large volcanic eruptions and ENSO events over AD 1525–2000. *Journal of Geographical Sciences* **30**, 103–118 (2020).
89. M. M. Dogar, T. Sato, Regional Climate Response of Middle Eastern, African, and South Asian Monsoon Regions to Explosive Volcanism and ENSO Forcing. *Journal of Geophysical Research: Atmospheres* **124**, 7580–7598 (2019).
90. C. E. Iles, G. C. Hegerl, A. P. Schurer, X. Zhang, The effect of volcanic eruptions on global precipitation. *Journal of Geophysical Research Atmospheres* **118**, 8770–8786 (2013).
91. R. K. Yadav, Why is ENSO influencing Indian northeast monsoon in the recent decades? *International Journal of Climatology* **32** (2012).
92. Z. Zhuo, I. Kirchner, S. Pfahl, U. Cubasch, Climate impact of volcanic eruptions: The sensitivity to eruption season and latitude in MPI-ESM ensemble experiments. *Atmos Chem Phys* **21**, 13425–13442 (2021).
93. N. Freychet, A. P. Schurer, A. P. Ballinger, L. Suarez-Gutierrez, C. Timmreck, Assessing the impact of very large volcanic eruptions on the risk of extreme climate events. *Environmental Research: Climate* **2**, 035015 (2023).
94. A. Parashar, S. Biswas, The impact of forest fire on forest biodiversity in the Indian Himalayas (Uttaranchal) in *XII World Forestry Congress*, (2003).